Development of a Dynamic Shielding Intensity Modulated Brachytherapy Applicator for the Treatment of Rectal Cancer

ALANA THIBODEAU-ANTONACCI

MEDICAL PHYSICS UNIT

MCGILL UNIVERSITY, MONTREAL

August, 2021

A thesis submitted to McGill University

in partial fulfillment of the requirements

for the degree of Master of Science

Abstract

High dose rate brachytherapy is a form of radiotherapy where a radioactive source is temporarily placed via catheters into or near the tumor. This close contact with the area to be treated allows a very efficient dose delivery. However, radiation sources used in conventional brachytherapy provide rotationally symmetric dose distributions, which often does not permit good tumor conformity. This can result in dose spillage to the surrounding radiation-sensitive organs, which increases the risk of negative side effects. By incorporating dynamically-rotating metallic shields around the brachytherapy source, intensity-modulated brachytherapy opens the possibility to deliver more conformal dose distributions.

Worldwide, colorectal cancer is the third most commonly diagnosed cancer in men and the second in women. Approximately a third of all colorectal cancer cases originate in the rectum. Surgical resection is the primary curative treatment for locally advanced rectal cancer, often combined with other treatment modalities like chemotherapy or radiotherapy. Preliminary results indicate that high dose rate brachytherapy is a good alternative to external beam radiotherapy in this context.

The goal of this project was to design and develop a dynamic shielding intensity-modulated brachytherapy applicator for the treatment of rectal cancer to reduce the dose received by the organs at risk while ensuring optimal irradiation of the tumor. This could significantly improve the curative potential of this treatment while simultaneously reduc-

ing toxicity and improving the quality of life of patients. Different shield designs were investigated using Monte Carlo simulations and a novel treatment planning system was used to find the best dose distribution for each patient. Results were compared with conventional high dose rate endorectal brachytherapy with and without static shielding. Radiochromic film and scintillator detector measurements were performed in solid water to validate the Monte Carlo code and determine the depth dose curve.

Résumé

La curiethérapie à haut débit de dose est une technique de radiothérapie qui consiste à insérer temporairement via des cathéters une source radioactive à l'intérieur ou à proximité de la tumeur. Ce contact direct avec la zone à traiter permet de délivrer des doses de radiation très efficacement. Cependant, les sources utilisées en curiethérapie conventionnelle émettent des rayonnements de façon sphérique ce qui ne permet pas de conformer la dose à la géométrie de la tumeur. Il en résulte que certains organes radiosensibles avoisinants sont irradiés, augmentant les risques de complications. En incorporant des blindages amovibles autour de la source, la curiethérapie à modulation d'intensité permettrait de délivrer des distributions de dose plus précises.

À l'échelle mondiale, le cancer colorectal est le troisième cancer le plus fréquemment diagnostiqué chez les hommes et le deuxième chez les femmes. Environ le tiers de tous les cas de cancer colorectal se développe dans le rectum. La résection chirurgicale est le traitement privilégié pour des tumeurs localement avancées, souvent accompagnée de chimiothérapie ou de radiothérapie. Des résultats préliminaires montrent que la curiethérapie à haut débit de dose est une bonne alternative à la radiothérapie externe dans ce contexte.

Le but de ce projet était de concevoir et de développer un appareil de curiethérapie à modulation d'intensité pour le cancer rectal afin de diminuer la dose reçue par les organes à risque tout en assurant une irradiation optimale de la tumeur. Ceci permettrait

d'augmenter le potential curatif de ce traitement tout en diminuant son niveau de toxicité et en améliorant la qualité de vie des patients. Différents modèles ont été étudiés grâce à des simulations Monte Carlo et un nouveau système de planification de traitement a été utilisé afin de trouver la meilleure distribution de dose pour chaque patient. Les résultats ont été comparés à la curiethérapie endorectale à haut débit de dose avec et sans l'utilisation de blindage statique. Des mesures ont été prises dans de l'eau solide avec des films radiochromiques et un scintillateur afin de valider le code Monte Carlo et déterminer le rendement en profondeur.

Acknowledgements

First, I would like to thank my supervisor, Dr. Shirin Abbasinejad Enger, for her guidance and encouragements during my studies. Also important is Dr. Té Vuong who provided useful advice and criticism. Thank you to Dr. Hamed Bekerat at the Jewish General Hospital without whom I could not have performed any experimental measurements. Additionally, I wish to thank Marc Morcos and Majd Antaki who helped build the Monte Carlo code and were there to answer all my questions. I would like to acknowledge all members of the Enger lab as well as my classmates at the Medical Physics Unit for their invaluable help. Special thanks to my family for their love and support!

Table of Contents

List of Figures

List of Tables

List of Abbreviations

AAPM	American Association for Physicists in Medicine
CTV	Clinical Target Volume
DVH	Dose-Volume Histogram
EBRT	External Beam Radiation Therapy
GBBS	Grid-Based Boltzmann equation Solver
HDR	High Dose Rate
HDREBT	High Dose Rate Endorectal BrachyTherapy
ICMA	IntraCavitary Mold Applicator
IMBT	Intensity-Modulated BrachyTherapy
LBTE	Linear Boltzmann Transport Equation
LDR	Low Dose Rate
MBDCA	Model-Based Dose Calculation Algorithm
MC	Monte Carlo
MDR	Medium Dose Rate
MRI	Magnetic Resonance Imaging
OAR	Organ At Risk
PDR	Pulsed Dose Rate
PDD	Percent Depth Dose
PSD	Plastic Scintillation Detector
TERMA	Total Energy Released per unit MAss
TPS	Treatment Planning System

Chapter 1

Background

1.1 Rectal Cancer

The World Cancer Research Fund reports that colorectal cancer is the third most common cancer in men and the second in women (World Cancer Research Fund, 2020). More specifically, in Canada, colorectal cancer is projected to account for 13% of new diagnoses and 12% of cancer related deaths in males in 2020. Comparatively, the incidence and mortality rates are 11% among females (Brenner et al., 2020). Rectal cancer makes up approximately one-third of all diagnosed cases, with the majority being adenocarcinomas (Tamas et al., 2015). Neoadjuvant chemoradiation followed by a total mesorectal excision is the mainstay of treatment in patients with locally advanced rectal cancer as it results in high rates of local control, sphincter preservation and patient survival. External beam radiotherapy (EBRT) is the most widely studied and used form of neoadjuvant radiation therapy in this context. This method delivers dose by aiming megavoltage x-rays or electrons from outside the body into the tumor. Yet, radiation-induced fibrosis increases the technical difficulty of the operation as well as the risk of surgical complications and locoregional recurrence. High dose rate brachytherapy, administered alone or as a boost to EBRT, is a safe alternative associated with comparable local control and survival rates, but

with lower incidences of treatment related toxicities due to a decreased dose to healthy surrounding tissues (Vuong, Devic, and Podgorsak, 2007; Vuong et al., 2010).

1.2 Brachytherapy

Brachytherapy is a form of radiation therapy where encapsulated radioactive sources are placed directly into or near the tumor to treat cancer. An important characteristic of this technique is the steep dose gradient close to the source which delivers a high dose to the target while limiting the exposure of surrounding organs at risk (OARs) (Chargari et al., 2019). The particles emitted by brachytherapy sources have a relatively low energy (average photon energy ranging from 0.021 MeV for Pd-103 to 1.25 MeV for Co-60) and thus have a shallow depth of penetration (half-value layer in lead ranging from 0.01 mm for Pd-103 to 11 mm for Co-60). Consequently, this treatment can only be used when the tumor is small and well localized (*e.g.*, gynecological, genitourinary and prostate cancers) (Podgorsak et al., 2005). Additionally, due to the rapid dose fall-off, there is a need for accurate delivery protocols and efficient quality control programs as small displacements of the source can result in significant dosimetric differences. However, contrary to EBRT, organ motion is typically not a problem in brachytherapy because the source is placed inside or near the tumor and will therefore maintain its position in relation to the target.

1.2.1 Type of implant

In brachytherapy, the dose can be delivered over a short period of time (temporary implants) or over the entire lifetime of the source (permanent implants). Treatments are classified according to the type of implant used. The two most common types of treatment are interstitial, in which the source is placed inside the tumor using needles, and intracavitary, in which the source is placed near the tumor using specialized applicators inside a body cavity (Podgorsak et al., 2005). The first can be temporary or permanent,

whereas the second is always temporary. Other forms of treatment use surface, intraoperative, intravascular or intraluminal sources.

1.2.2 Source loading

There are two types of source loading: hot loading and afterloading. The first is when the brachytherapy applicator is preloaded and contains the radionuclide at the time of placement inside the patient. This source loading method can be used for low dose rate seeds (such as in an eye plaque), but is rarely performed in the clinic for radiation safety reasons. Instead, afterloading is generally used and the source is loaded after the applicator is placed inside the patient, either by hand (manual afterloading) or by a machine (remote afterloading). Manual afterloading has largely been replaced by remote afterloading, where a machine automatically pushes the source to specific prescribed positions (dwell positions) with different irradiation times (dwell times) (Podgorsak et al., 2005). This technique has the advantage of minimizing the radiation exposure of the medical staff. Both loading methods are available for permanent and temporary implants.

1.2.3 Dose rate

Brachytherapy treatments are commonly classified with respect to dose rate at the point or surface where the dose is prescribed (Chassagne et al., 2016). Low dose rate (LDR) devices emit a dose rate between 0.4 and 2 $\mathrm{Gy\,h^{-1}}$ and can be loaded manually or remotely. For temporary implants, treatment duration varies between a few hours to a few days, and the patient typically stays in the hospital during that time. LDR is also compatible with permanent implants. Medium dose rate (MDR) brachytherapy corresponds to a dose rate between 2 and 12 $\mathrm{Gy\,h^{-1}}$. This type of treatment is not commonly used in the clinic as treatment results are poor compared with other methods. Finally, high dose rate (HDR) brachytherapy delivers a dose rate greater than 12 $\mathrm{Gy\,h^{-1}}$. The most common isotope used is Ir-192, which emits a dose rate greater than 2 $\mathrm{Gy\,min^{-1}}$. A remote afterloader

is used in this case for staff safety (Podgorsak et al., 2005). The dose distribution in HDR brachytherapy is optimized in a treatment planning system (TPS) by varying the dwell positions and dwell times. Because of this, the delivered dose more closely resembles the planned dose. Indeed, contrary to LDR brachytherapy, this modality is not susceptible to seed misplacement or movement. As a result, target coverage and normal tissue sparing are generally more consistently achieved. Furthermore, HDR brachytherapy has some cost benefits as the source is used to treat multiple patients as long as it has an acceptable activity (Morton and Hoskin, 2013).

Alternatively, pulsed dose rate (PDR) brachytherapy systems are programmed to deliver short HDR pulses at hourly intervals to simulate a continuous LDR treatment. This technique combines the physical advantages of HDR technology with the radiobiological advantages of LDR brachytherapy (Visser, Aardweg, and Levendag, 1996). However, recent studies, mainly performed for cervical cancer, have found no significant difference in biological effects between LDR and HDR brachytherapy (Hannoun-Levi, 2017). Moreover, the organization management of PDR brachytherapy resembles that of LDR treatments, while HDR brachytherapy is comparable to EBRT. In brief, the choice treatment method must be made on a case by case basis taking into account biological, technological, organizational and financial considerations.

1.2.4 Dosimetry

Convention brachytherapy dosimetry is based on the American Association for Physicists in Medicine (AAPM) Task Group No. 43 report, referred to as TG-43 (Nath et al., 1995; Rivard et al., 2004). The TG-43 dose calculation formalism describes dose delivery around a single photon emitting source positioned at the center of a spherical water phantom. For a cylindrically symmetric source, the rate of absorbed dose to water can be described in the polar coordinate system with the origin at the center of the source. It is given by the following equation:

$$\dot{D}(r,\theta) = S_K \cdot \Lambda \cdot \frac{G_X(r,\theta)}{G_X(r_0,\theta_0)} \cdot g_X(r) \cdot F(r,\theta) \tag{1.1}$$

where r corresponds to the distance (in centimeters) to the point of interest, denoted as P(r, θ) in Figure 1.1, and θ is the polar angle relative to the source longitudinal axis. The reference point, P(r_0, θ_0), is located 1 cm away from the source center at 90°. The subscript "X" indicates whether a point source ("P") or a line source ("L") model is used. The dose distribution is assumed to be symmetric with respect to the transverse plane. However, the above equation can be modified to accommodate non-symmetrical sources.

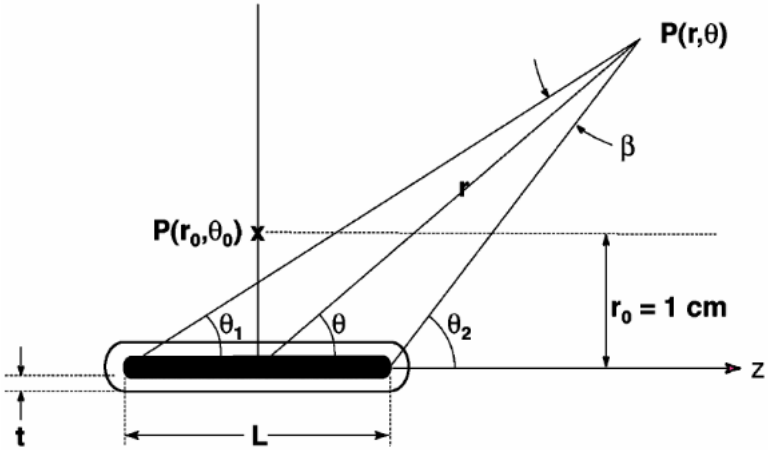

Figure 1.1: Coordinate system used for brachytherapy dosimetry calculations (Rivard et al., 2004).

The air-kerma strength, S_K, is defined as the air-kerma rate, $\dot{K}_\delta(d)$, in vacuum at a distance d and due to photons of energy greater than δ, multiplied by the distance squared:

$$S_K = \dot{K}_\delta(d) \cdot d^2 \tag{1.2}$$

The units are 1 U = 1 μGy m^2 h^{-1} = 1 cGy cm^2 h^{-1}. The distance d must be large relative to the dimensions of the source so that S_K is independent of d. $\dot{K}_\delta(d)$ is determined by measuring the air-kerma rate in free-air at 1 m from the source center and correcting

the obtained value for photon attenuation and scattering in air and in any other material present between the source and detector. The energy cutoff, δ, eliminates low-energy and contaminant photons that increase the air-kerma rate without significantly contributing to the dose at distances greater than 1 mm in tissue. For low-energy photon-emitting brachytherapy sources, δ is generally equal to 5 keV.

The dose rate constant in water, Λ, corresponds to the ratio of the rate of absorbed dose to water at the reference point and S_K:

$$\Lambda = \frac{\dot{D}(r_0, \theta_0)}{S_K} \tag{1.3}$$

The units are 1 cGy h^{-1} U^{-1} = 1 cm^{-2}. This parameter depends on the source radionuclide and geometry. It is obtained from Monte Carlo (MC) simulations or direct measurements. In fact, the AAPM Low-energy Interstitial Brachytherapy Dosimetry subcommittee recommends using an equally weighted average of measured and calculated values for each source model.

The geometry function, G_X(r, θ), is an effective inverse square-law correction used to interpolate the dose rate between tabulated values measured at specific points:

$$G_P(r, \theta) = r^{-2} \tag{1.4}$$

$$G_L(r, \theta) = \begin{cases} \frac{\beta}{Lrsin\theta} & \text{if } \theta \neq 0° \\ \frac{1}{r^2 - L^2/4} & \text{if } \theta = 0° \end{cases} \tag{1.5}$$

where L is the active length of the line source and β is the angle subtended by the tips of the line source with respect to the point of interest (Figure 1.1). The geometry function neglects the effects of scattering and attenuation. The units are cm^{-2}.

The radial dose function, g_X(r), accounts for the dose fall-off on the transverse axis due to photon scattering and attenuation. It is given by:

$$g_X(r) = \frac{\dot{D}(r,\theta_0)}{\dot{D}(r_0,\theta_0)} \frac{G_X(r_0,\theta_0)}{G_X(r,\theta_0)} \tag{1.6}$$

A mathematical model fit to tabulated values of g_X(r) permits the interpolation of this parameter at any distance from the source center.

The 2D anisotropy function, F(r, θ), describes the dose variation according to the polar angle and is defined as:

$$F(r,\theta) = \frac{\dot{D}(r,\theta)}{\dot{D}(r,\theta_0)} \frac{G_L(r,\theta_0)}{G_L(r,\theta)} \tag{1.7}$$

For a point source, the dose rate is independent of θ such that the anisotropy function is equal to unity. TG-43 recommends MC derived anisotropy functions as this method generates smoother datasets with higher spatial and angular resolution as well as a greater distance range. These functions have been validated by comparison to experimental data.

The AAPM TG-43 has standardized brachytherapy dosimetry and permitted easy comparison between institutions. An important advantage of the analytical formulation presented in the report is that it leads to fast and consistent dose computation. Furthermore, the values of the various parameters are compiled following a rigorous process. However, patient geometry, tissue composition and density heterogeneities are ignored, which may lead to inaccuracies and inconsistencies between the prescribed dose and the delivered dose in some cases. This will be further discussed in the next section.

1.3 Model-based dose calculation

Contrary to EBRT, material heterogeneity corrections are generally not applied in brachytherapy dosimetry. However, for low- and intermediate-energy sources, the all-water approximation made by the TG-43 formalism is poor and can lead to significant differences in calculated dose compared with model-based dose calculation algorithms (MBDCAs) because the photoelectric effect is dominant at these energies. Indeed, the mass attenuation coefficient of this process is highly dependent on the atomic number of the attenuating material and the energy of the photon (Podgorsak et al., 2005). Although this effect is less important for high-energy sources, previous studies have shown considerable deviations in dose metrics for OARs (Poon et al., 2008; Shoemaker et al., 2019).

Moreover, the use in certain cases of high-density materials for static or dynamic shielding further increases the need for more accurate geometrical descriptions of the patient and implanted applicators. In these situations, MBDCAs result in more accurate dose calculation as they account for all sources of scatter and heterogeneities. However, they are subject to notable variations in the predicted dose depending on the way imaging and applicator structure data are obtained and used. Thus, the AAPM Task Group No. 186 report (TG-186) provides guidance for the clinical adoption of MBDCAs for brachytherapy dosimetry (Beaulieu et al., 2012). In particular, the report addresses the choice of dose specification medium, voxel-by-voxel cross-section assignment as well as commissioning procedures for MBDCAs. In summary, authors recommend the reporting of dose to the tissue composing each voxel rather than to a fixed reference medium such as water. They also suggest that the tissue composition of a given organ be assigned uniformly to the contour approved by the radiation oncologist. Tables of material definitions are provided. If CT data are available, CT derived densities should be used. However, a study by Shoemaker *et al.* found that the calculated dose distribution is not significantly affected by the loss of voxel-wise CT density data as long as elemental compositions and

nominal mass densities are correctly assigned to each contour (Shoemaker et al., 2019). This is important as magnetic resonance imaging (MRI)-based brachytherapy treatment planning is gaining traction due, in part, to its greater soft-tissue contrast. HU density data for each voxel is unavailable in MRI-based dosimetry. Finally, any TPS using an MBDCA should allow direct comparison with consensus TG-43 parameters by calculating the dose or dose rate in a homogeneous water phantom.

MBDCAs are broadly divided into semiempirical and first-principal approaches. Algorithms belonging to the first category are less accurate but generate brachytherapy treatment plans in the same timescales as conventional TG-43-based methods. On the other hand, first-principal approaches either explicitly simulate the transport of radiation in matter or use multidimensional scatter integration techniques to account for the dependence of scatter dose on the 3D geometry (Beaulieu et al., 2012). Three major examples of this type of algorithm are collapsed-cone superposition/convolution, deterministic solutions to the linear Boltzmann transport equation (LBTE) and MC simulations. The first calculates the dose distribution by performing the convolution of the Total Energy Released per unit MAss (TERMA) and kernels mapping the energy deposition from an interaction point in water. These kernels are precalculated with MC (Victor, 2015). Ray tracing is used to account for heterogeneities by scaling the radiation path by the density of the medium. In EBRT treatment planning, two kernels are used to represent the primary and scatter dose. The collapsed cone approximation, which assumes that the energy released into coaxial cones of equal solid angle is entirely deposited in voxels on the cone axis, increases the calculation efficiency. Alternatively, deterministic methods iteratively solve the linear system of equations obtained by discretizing spatial, angular and energy variables of the LBTE. TG-186 groups these approaches as grid-based Boltzmann equation solvers (GBBS) because they are based on phase-space discretization (Beaulieu et al., 2012). Finally, MC simulations use random sampling to solve the LBTE. This approach can be summarized in three steps:

1. Calculate the distance to the next interaction given the linear attenuation coefficient of the medium.

2. Determine the interaction type by sampling the relative magnitude of each cross-section.

3. Simulate the interaction to obtain the energy and direction of the primary and secondary particles.

These steps are repeated until all particles are absorbed or leave the defined geometry. The absorbed dose per voxel is estimated as the average over all histories ($\bar{D}$). In the context of brachytherapy dosimetry, the term history refers to the process of simulating a primary particle and all the secondaries produced by it. The central limit theorem states that in the limit N $\rightarrow \infty$ the probability distribution of $\bar{D}$ is Gaussian. As such, the variance of this value is given by:

$$s^2 = \frac{1}{N}\left(\frac{\sum i q_i^2}{N} - \bar{q}^2\right) \tag{1.8}$$

where N is the number of histories (Sempau et al., 2001). The standard deviation corresponds to the square root of the variance. The above equation shows that the statistical uncertainty decreases as the number of histories increases. MC models are the gold-standard for dosimetry, but they are not traditionally used in the clinic because of their high computational cost (Victor, 2015).

No matter the type of MBDCA dose engine used, there is a trade-off between computational speed and dose calculation precision. Therefore, a certain amount of uncertainty will be associated with the obtained result. To ensure sufficiently accurate dose predictions, new code implementations must be benchmarked against MC or experimental results when possible.

1.4 High dose rate endorectal brachytherapy

At the Jewish General Hospital (Montreal, Canada), CT-based image-guided adaptive high dose rate endorectal brachytherapy (HDREBT) is performed on patients with locally advanced rectal cancer using an Ir-192 source (Nout et al., 2016). It can be given alone as a pre-operative treatment in four daily fractions of 6.5 Gy, or as a boost to EBRT in three weekly fractions of 10 Gy. Before the first treatment, patients undergo a proctosigmoidoscopy to visualize the lesion and place radio-opaque clips around its periphery. This facilitates target delineation during treatment planning. At the time of treatment, a digital rectal examination is carried out to assess the angle of the anal canal as well as the distance of the tumor from the anal verge. A proctosigmoidoscopy can also be repeated to verify the position of the lesion relative to the clips. During this procedure, the size of the tumor, which may change between brachytherapy fractions, is taken into account for adaptive treatment. All of this information is combined and a cylindrical intracavitary mold applicator (ICMA) (Nucletron/Elekta; Veenendaal, the Netherlands) is inserted inside the rectum (figure 1.2). The rectal applicator is 28 cm long and 2 cm in diameter. It contains eight catheter channels equally distributed around a 8 mm diameter central lumen and is made of a flexible silicon rubber for easy insertion. For nonobstructing semicircumferential lesions, a balloon can be placed over the applicator opposite the tumor to increase the distance between the source and the healthy contralateral rectal wall (Nout et al., 2016). Additionally, a second balloon ipsilateral to the target can be used to compress the tumor. This allows better dose conformity by decreasing the dose gradient within the lesion (Devic et al., 2019). Both balloons are filled with varying volumes of iodine contrast medium and permit better fixation of the applicator.

After positioning, a CT scan with a small number of thick slices (3 - 5 mm) is performed over the entire treatment volume to verify the applicator position relative to the clips and all the necessary adjustments are made. Next, another CT scan with a greater

number of slices is taken for contouring and treatment planning. Radio-opaque markers placed in three catheter channels allow accurate applicator reconstruction and determination of the first dwell position.

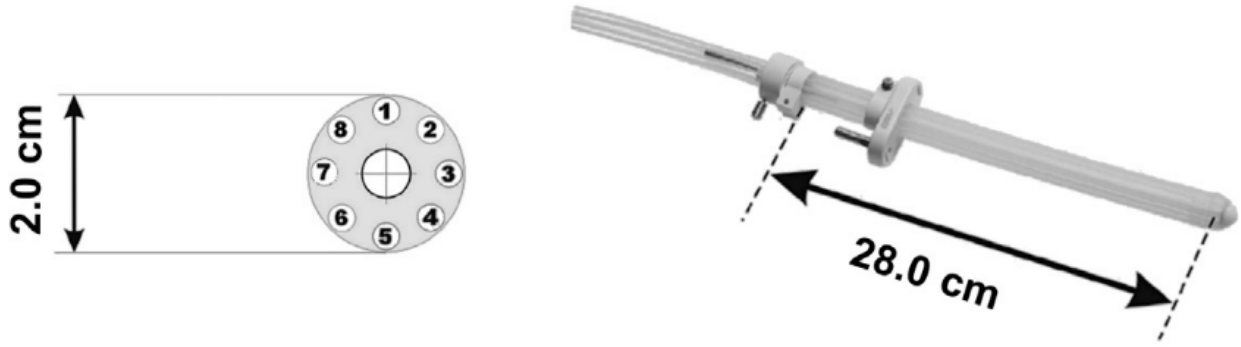

Figure 1.2: Intracavitary mold applicator used for high dose rate endorectal brachytherapy. Catheters 1, 3 and 7 are engaged with x-ray markers for applicator reconstruction.

Dose optimization is usually done with an inverse planning software taking into account dose constraints to the tumor and surrounding OARs. The dose-volume histogram (DVH) represents the most common tool for evaluating treatment plans. Before treatment delivery, a tungsten or lead rod can be inserted in the central lumen of the applicator for additional healthy tissue sparing on the contralateral side. However, this is only possible in cases where three consecutive catheter channels or less are used for treatment. For bigger tumors, the prescribed dose distribution to the target might be compromised (Nout et al., 2016). A previous study has shown with ionization chamber measurements in a Lucite phantom that the use of a tungsten rod attenuates the dose by up to 85% in the shielded region (Poon et al., 2006). The experimental results agreed with MC simulations within measurement uncertainties.

1.5 Intensity-modulated brachytherapy

An important limitation of brachytherapy is the rotationally symmetric dose distribution provided by conventional sources, which delivers a high dose to the tumor but often with poor target conformity due to the irregular shape of the lesion. This results in dose spillage to the peripheral radiation sensitive tissue (Callaghan et al., 2019; Famulari, Duclos, and Enger, 2020; Morcos and Enger, 2020). By incorporating highly attenuating material inside the brachytherapy applicators, it is possible to direct the radiation beam towards the tumor and away from OARs (Figure 1.3). This is the principle behind intensity modulated brachytherapy (IMBT), a novel brachytherapy treatment modality that uses static or dynamic metallic shields. The idea of IMBT was first investigated by Ebert in 2002 (Ebert, 2002). They concluded that a collimation angle between $\pi/8$ to $\pi/4$ and a transmission through the shield of less than 10% are necessary to observe significant advantages of this method compared with conventional HDR brachytherapy.

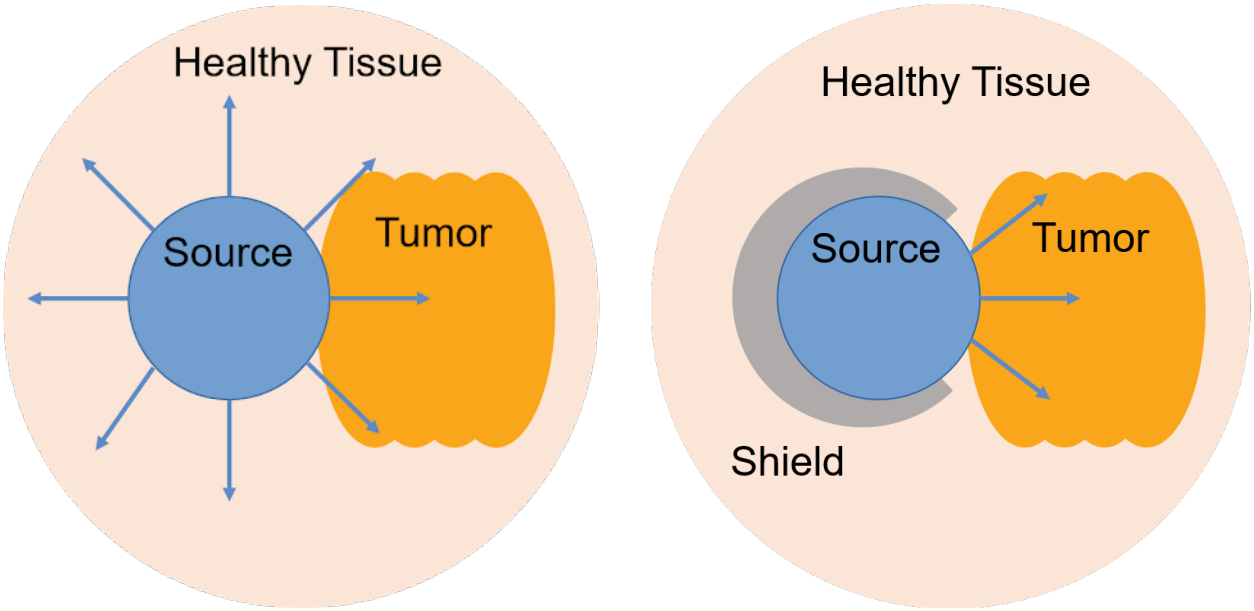

Figure 1.3: Schematic representation of the radiation beams emitted by a brachytherapy source (a) without and (b) with shielding.

Static shielding IMBT includes all designs where the shield is immobile relative to the source or surrounding tissues during treatment. The delivery times are comparable to standard multichannel brachytherapy applicators. The device currently employed for endorectal brachytherapy at our institution can house a static metallic shield for organ sparing. However, as mentioned previously, only three catheter channels can be used for source loading with active dwell positions within 5 mm of the inner clinical target volume (CTV) border. Consequently, only patients with relatively small tumors can benefit from static shielding with this applicator. In contrast, dynamic shielding IMBT methods permit the rotation and translation of the shield relative to the source or surrounding tissues, which creates a highly collimated field in all directions (Webster et al., 2013a). However, important limitations of these designs include longer treatment times as well as a greater complexity of the setup and delivery. This makes their implementation in the clinic more difficult (Callaghan et al., 2019).

1.6 Radiochromic film

Radiochromic film is a powerful 2D dosimetry tool for radiotherapy quality assurance and treatment verification purposes. The EBT3 Gafchromic film model consists of a 28 μm thick active layer containing a matrix of di-acetylene dye monomers sandwiched between two 125 μm thick matte polyester layers. When a piece of radiochromic film is irradiated, charged particles initiate the polymerization of the sensitive layer. This results in a change in optical density proportional to the amount of energy deposited that can be measured using a flatbed document scanner (Devic, Tomic, and Lewis, 2016). EBT3 films are recommended for use in a dose range of 0.01 Gy to 30 Gy. Furthermore, embedded silica particles within the outer layers prevent the formation of Newton rings interference patterns in scanned images.

Radiochromic films present numerous advantages that make them ideal for measurements in fields with high dose gradients. Namely, they are near tissue-equivalent, have a high spatial resolution and a relatively small energy dependence. In order to determine an unknown dose, a calibration curve relating optical density to known doses must first be measured. Because the film response is dependent on its orientation, it is important that the film pieces used for calibration and measurement be handled and analyzed the same way.

1.7 Scintillator detectors

Scintillators are materials that emit low energy photons when they are exposed to ionizing radiation. They are divided in two main categories: organic and inorganic. Plastic organic scintillators are the most widely used and will be the focus of this section. A plastic scintillation detector (PSD) is typically composed of the scintillator itself, which corresponds to the sensitive region, a light guide and a photodetector (Figure 1.4). The latter converts the visible light produced by the sensitive volume into numerical signal (Beddar et al., 2021). In radiation therapy applications, PSDs measure the relative dose delivered at a given point by a radiation beam, which is generally proportional to the number of emitted scintillation photons. They use a small volume scintillator in order to maximize their spatial resolution. An important challenge of PSDs is the Cerenkov radiation emitted by all clear components of the detector that contaminate the signal. Cerenkov light is a luminescence signal produced by charged particles travelling faster than the phase velocity of light in a dielectric medium. However, there exists different strategies to mitigate this effect, such as the spectral method.

Cavity theories or MC simulations are used to relate the dose measured by the scintillator in a phantom to the dose that would be received in that same region in the absence of the dosimeter. This conversion is greatly simplified if the composition of the detector

closely matches the composition of the medium. For this reason, plastic scintillator generally are composed of low Z materials with a density close to that of water, which is the reference medium in radiation therapy (Beddar et al., 2021).

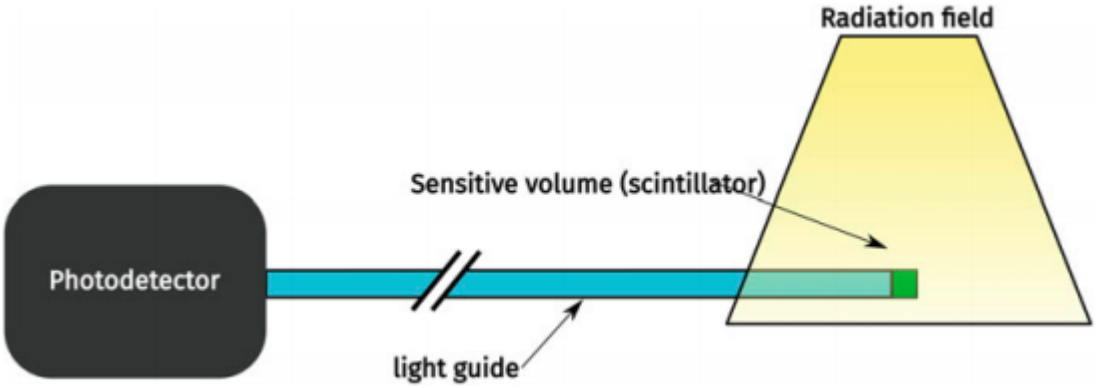

Figure 1.4: Schematic showing a common measurement setup with a plastic scintillation detector. Image taken from (Beddar et al., 2021).

1.8 Objectives

The purpose of this work was to develop a novel MRI-compatible dynamically-rotating shield for intensity-modulated endorectal brachytherapy. This could permit more conformal dose distributions. The first goal was to assess the uninvolved tissue sparing capacity of our applicator by optimizing and calculating the absorbed dose to the tumor and surrounding OARs with a MC-based treatment planning system. The results were compared to conventional HDREBT with and without static shielding. A secondary aim was to test the radiation attenuation capacity of our shield with radiochromic film and scintillator detector measurements in solid water.

Chapter 2

Materials and methods

This chapter describes the dynamically-rotating IMBT shield design as well as the MC-based treatment plans generated to validate its healthy tissue sparing properties. The same patients were also planned using the conventional HDREBT applicator with and without static shielding for comparison. Additionally, the experimental measurements performed with a prototype of the shield are presented.

2.1 Dynamically-rotating IMBT shield design

The first version of the endorectal dynamically-rotating IMBT shield (referred hereafter only as the shield) was a 15 mm diameter single-grooved cylinder with a 2 mm source channel positioned at the center to permit the insertion of a 6F catheter (Figure 2.1). The emission window was 2 mm. The length of the shield had to be optimized so that it could fully cover any target, but still be relatively light for patient comfort. Therefore, based on the dimensions of a sample of rectal tumors, the length was set to 8 cm. In the future, this parameter will be adjusted according to the size of a greater number of tumors. Tungsten alloy was the preferred material because of its low magnetic susceptibility, making it MRI-compatible, and high density (ρ = 19.3 g cm^{-3}). Previous evidence has shown that this material efficiently attenuates the radiation beam and strikes a good balance between

manufacturability and affordability (Poon et al., 2008; Safigholi et al., 2018). Treatment plans with the first shield design were calculated using MC for two rectal cancer patients that each received three fractions of brachytherapy. Treatment plans were also generated using an 18 mm diameter shield with similar characteristics.

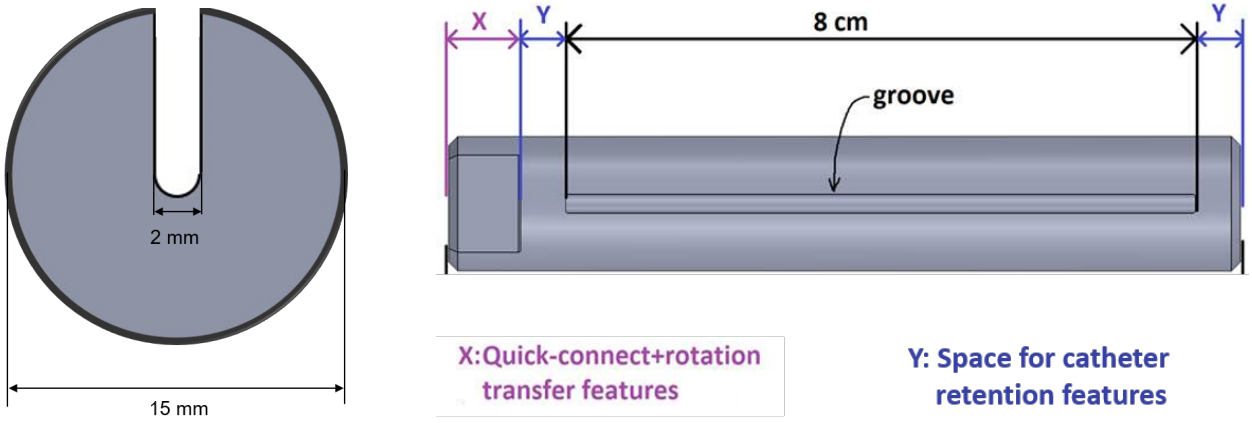

Figure 2.1: (a) Front view and (b) side view of the initial endorectal IMBT shield design.

Alternate shield designs with increasing emission windows were also explored with the goal to decrease the overall treatment time. In the end, the shield design that generated the best treatment plans with satisfactory treatment times had an 180° emission window (Figure 2.2). All other characteristics (diameter, length, material, etc.) were kept the same as the previous model.

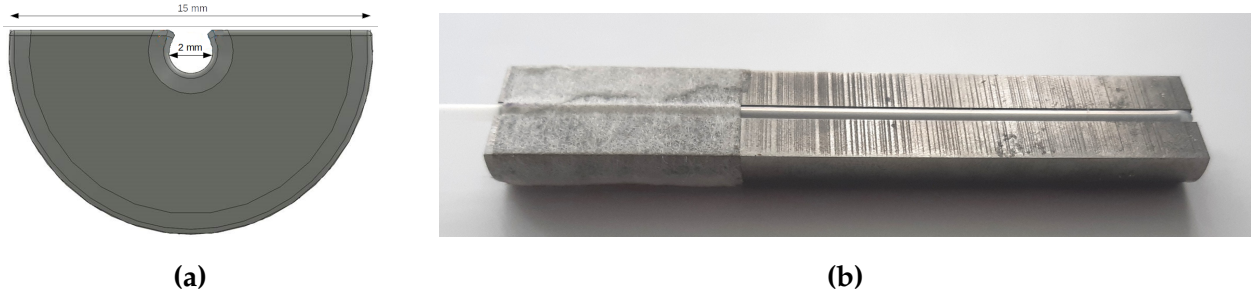

Figure 2.2: (a) Front view and (b) prototype of the final endorectal IMBT shield design.

During treatment, the shield will be fitted in a pliable silicon applicator to facilitate insertion into the rectal lumen. This will also avoid tearing the delicate lining of the organ. Furthermore, to facilitate the transition to the clinic, the applicator will be attached to a rotating delivery system compatible with any commercial HDR afterloader as an add-on device. This delivery system was presented in previous works (Famulari, Duclos, and Enger, 2020; Famulari and Enger, 2018). In brief, in consists of a rotating mechanism, a joint assembly and a shield assembly (Figure 2.3). The device controls the rotation of the shield during treatment while the afterloader drives the radiation source to the correct dwell positions. The necessary software that connects the TPS to the delivery system still needs to be developed.

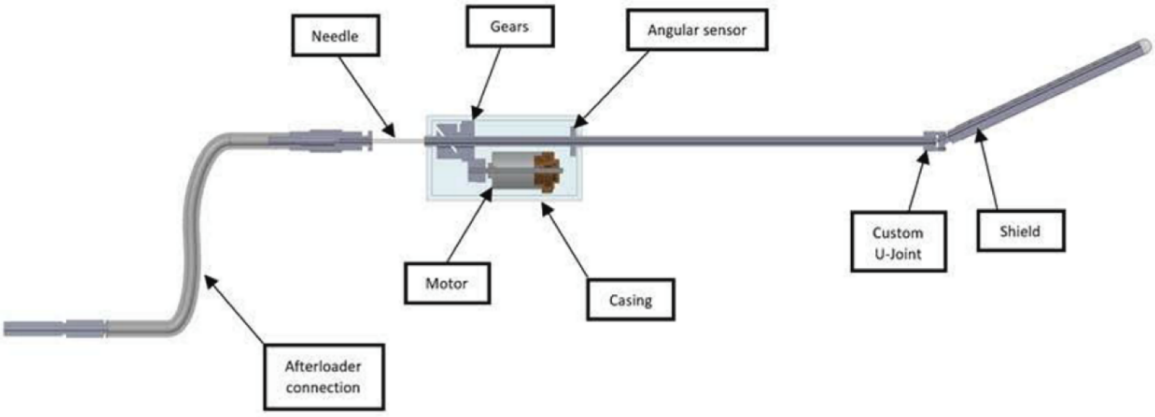

Figure 2.3: Prototype delivery system for dynamic shielding IMBT that can connect to an HDR afterloader. Image taken from (Morcos and Enger, 2020)

2.2 Monte Carlo simulations

2.2.1 Patient dataset

Four HDREBT boost patients treated at the Montreal Jewish General Hospital were included in this study. The prescribed dose to the tumor was 10 Gy per fraction. Patient data were anonymized and CT images were taken from each treatment fraction in DICOM

format. The CTV, contralateral healthy rectal wall and dose spill regions 1 cm above and below the target were segmented. These contours do not represent any physical structures, but are used to limit and evaluate the dose leakage around the applicator. They are shown in Figure 2.4. The CTV length was determined by multiplying the number of slices where the tumor was contoured by the slice thickness (3 mm). Therefore, this value is an approximation limited by the resolution of the CT scan in the longitudinal direction. Different surrounding organs (rectum, bladder, femur and pelvis) were also contoured.

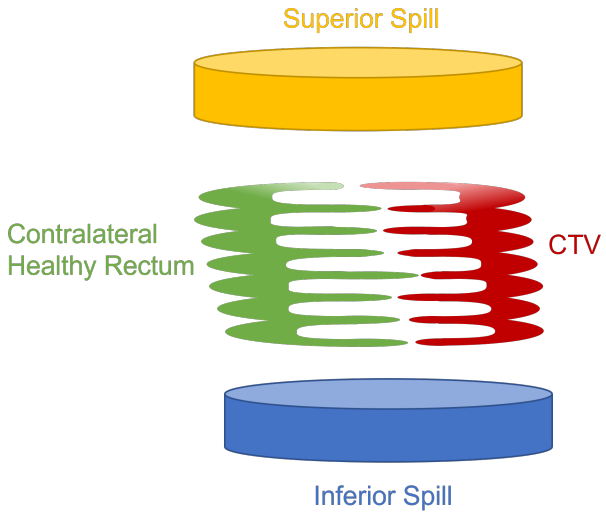

Figure 2.4: Structures contoured for treatment planning: CTV (red), contralateral healthy rectal wall (green), superior dose spill region (yellow) and inferior dose spill region (blue).

2.2.2 HDR source

A generic Ir-192 HDR source was simulated. The cylindrical active core (0.6 mm diameter and 3.5 mm length) was contained in a stainless-steel-316L capsule measuring 1.0 mm in diameter and 4.6 mm in length. The drive cable was composed of stainless-steel-316L5 and had outer dimensions of 1.0 mm diameter and 2.0 mm length.

2.2.3 Treatment plan

Conventional HDREBT plans with and without static shielding were retrospectively calculated with RapidBrachyMCTPS, an open source MC-based research treatment planning system developed at our institution that was previously validated against other available MC brachytherapy codes by comparing TG-43 parameters for Ir-192 and I-125 source models (Famulari et al., 2018; Glickman et al., 2020). In both cases, dwell positions were created in the three consecutive catheter channels closest to the tumor. The distance between consecutive dwell positions was 5 mm. Tissue elemental compositions were assigned to relevant contours based on the recommendations of TG-186 (Beaulieu et al., 2012) and nominal physical densities taken from ICRU Report No. 46 (Bethesda, 1992) were used (Table 2.1). For static shielding HDREBT, the central lumen of the applicator was contoured on pre-treatment CT images and assigned as tungsten alloy. Dynamic shielding IMBT plans were also generated in RapidBrachyMCTPS. Using the parallel world formalism implemented in Geant4 (Enger et al., 2012), the tungsten shield was placed in the center of the intracavitary mold applicator in clinical pre-treatment CT images and dwell positions were created along the central source channel. The shield rotation was limited to 15° increments.

Material	Density (g/cc)	Element (% mass)											
		H	C	N	O	Na	Mg	P	S	Cl	Ar	K	Ca
Air	0.001225		0.0124	75.5268	23.1781						1.2827		
Soft Tissue	1.02	10.6	31.5	2.4	54.7	0.1		0.2	0.2	0.1		0.2	
Rectum	1.03	10.6	11.5	2.2	75.1	0.1		0.1	0.1	0.2		0.1	
Bladder (filled)	1.03	10.8	3.5	1.5	83.0	0.3		0.1	0.1	0.5		0.2	
Cortical Bone	1.92	3.4	15.5	4.2	43.5	0.1	0.2	10.3	0.3				22.5

Table 2.1: Density and elemental composition of tissue types.

2.2.4 Dose calculation

CT images were converted to voxelized phantoms in egsphant format with voxel size 3 x 3 x 3 mm^3. Macro files for each dwell position and shield angle combination were then created and imported to Béluga, a remote general purpose cluster provided by Compute Canada. For optimization, 10^6 decay events were simulated using the Geant4 radioactive decay module. Photons were tracked using the PENELOPE electromagnetic physics list with default transport parameters. The assumption that secondary electrons deposit their energy locally was made due to the relatively low photon energy emitted by the source radionuclide (average energy of 355 keV). Indeed, supposing a 355 keV photon transfers all of its energy to an orbital electron, the "continuous slowing down approximation" range, defined as the mean path length along the particle's trajectory, is 1.07 mm in soft tissue according to a database published by NIST. The maximum penetration depth approaches half of this value, meaning the electron won't exit a 1 x 1 x 1 mm^3 voxel most of the time. Although some photons have a higher energy than 355 keV, they represent only of a fraction of the total spectrum. Therefore, dose was approximated to collision kerma and scored using a track length estimator which accelerated the calculation (Williamson, 1987). Multithreading was was also used to decrease the computation time: histories were divided among 40 CPUs. Type A uncertainty on the absorbed dose per voxel was calculated using the history-by-history method presented in Equation 1.8.

2.2.5 Dose optimization

The resulting individual dose distributions were imported back to RapidBrachyMCTPS and used as input for the fast mixed integer optimization algorithm. Minimum and maximum dose constraints as well as their weights were defined for the target and OARs, respectively. The objective function used by the optimization algorithm contains a linear part and two quadratic parts (Antaki, Deufel, and Enger, 2020). The linear component is a one-sided penalty for deviations from the dose constraint. Similarly, the first quadratic

part is a one-sided penalty but with a focus on the DVH tail in the OARs and the DVH shoulder in the target. Minimizing this penalty permits a better CTV coverage and reduced dose to the OARs. The second quadratic component is a two-sided penalty for any differences from the prescribed dose in the tumor. A more uniform dose distribution in the target (*i.e.*, fewer hot spots) can be achieved by minimizing this part of the equation. In general, voxels belonging to the tumor volume will be penalized if they receive less than the prescribed dose. On the contrary, voxels that comprise the OARs will be penalized for doses higher than the set limit.

The maximum dose limit to the OARs and their weights were manually adjusted until the optimization algorithm produced a treatment plan where the CTV D_{90} received within 1% of the prescribed dose. A single macro file containing information on all the dwell positions and dwell times was created and imported to Béluga. The final dose distribution was calculated with 10^9 decay events and a 1 x 1 x 1 mm^3 scoring grid to reduce the Type A uncertainty under 0.5% for voxels inside the 100% isodose lines. For dynamic shielding IMBT, the dose to the tumor was less than the prescribed value for five cases. To correct this, the dose distributions per dwell position and shield angle combination were calculated again with 10^7 histories and the optimization step was repeated.

2.2.6 Plan comparison indices

The uninvolved contralateral rectal D_{2cc}, superior dose spill region D_{2cc} and inferior dose spill region D_{2cc} were compared by normalizing the clinical and IMBT plans such that the CTV $D_{90\%}$ received 10 Gy per fraction. Additionally, the $D_{50\%}$ was determined for the rectum, bladder, femur and pelvis. $D_{x\%|xcc}$ is defined as the minimum dose received by the hottest x% or x cm^3 of the structure volume. Difference in DVH metrics were evaluated using a paired two-sided t-test. A P-value smaller than 0.05 was considered statistically significant.

2.3 Radiochromic film measurements

A prototype of the 180° emission window dynamically-rotating IMBT shield was built with the help of our commercial partners (Pega Medical, Quebec, Canada). Measurements with Gafchromic EBT3 films (Ashland Inc., Wayne, NJ) were carried out in solid water (Gammex, Middleton, WI) to validate the MC code and demonstrate the safety of the device by testing for any radiation leakage. Analysis was performed with a flatbed Epson Expression 11000XL document scanner (Seiko Epson Corporation, Nagano, Japan) that provides 48-bit RGB images. Both the calibration and measurement films were scanned approximately 24 hours after irradiation with 127 dpi which corresponds to 0.2 mm/pixel. To minimize light diffusion artifacts, the area of interest was limited to a 10 x 10 cm^2 square in the center of the scanner. Rotation of the film on the scanner bed leads to significant differences in measured signal. Therefore, all films were labeled and scanned in the portrait orientation (Aldelaijan et al., 2011).

2.3.1 Film calibration

Calibration films were irradiated on a TrueBeam linac (VarianMedical Systems, Palo Alto, CA) with 6 MV photons to varying doses (0, 0.25, 0.50, 1, 2, 4, 6, 8, 10, 12, 15, 20, 25, 30 and 35 Gy). The films were placed between 1.5 cm blocks of solid water in the center of a 10 x 10 cm^2 field. The source to surface distance was set to 100 cm. After irradiation, the films were digitized and the mean pixel value as well as its standard deviation were extracted from a central region of interest. A calibration curve characterizing the pixel value as a function of dose was created for each color channel by fitting a rational function to the data (Lewis et al., 2012). Figure 2.5 shows these curves. The differences between the measured and fitted pixel values and dose data are also presented. Based on the small dose residual at higher doses, the green channel was used for further analysis.

Calibration and experimental measurements with the IMBT shield prototype were performed with different beam qualities. This raises questions regarding the Type B uncertainties related to the small energy dependence of radiochromic film. However, the EBT3 film model has shown to be energy independent for photon energies greater than 400 keV (Devic, Tomic, and Lewis, 2016). Moreover, the addition of aluminium in the active layer matrix further improved the energy response of the latest commercial iteration. In fact, a 2014 study has shown that the film's under response was within 5% at 50 keV effective photon energy (Bekerat et al., 2014). Therefore, the above calibration method was deemed acceptable.

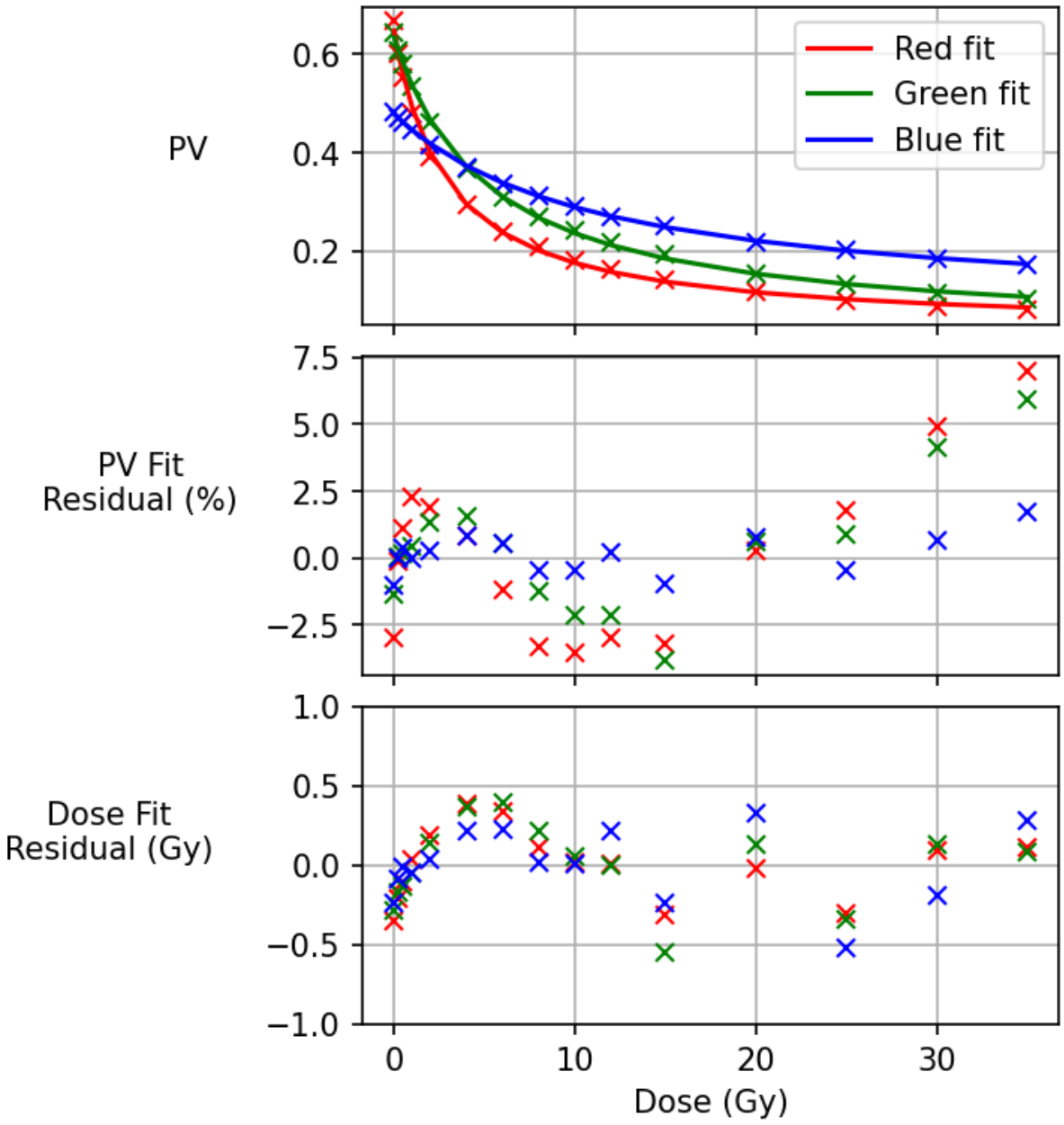

Figure 2.5: Calibration curve for each color channel (top), pixel value percent difference (middle) and dose difference (bottom). PV = pixel value.

2.3.2 Measurement of the dose distribution

The 2D dose distribution at different distances from the shield was measured by placing 8 x 8 cm^2 squares of radiochromic film between blocks of solid water as presented in figure 2.6. The microSelectron Ir-192 HDR v2 source (Nucletron, Veenedaal, The Netherleands) was used with a single dwell position at the center of the shield. Contrary to the image below, measurements were performed in two steps. First, the films were placed on the shielded side and the dwell time was set to 400 seconds so that the films received enough dose. Bolus was used to fill any air gaps around the shield. Then, the shield was turned 180° and new films were placed to determine the dose distribution on the unshielded side. The dwell time was decreased to 45 seconds to avoid saturating the film.

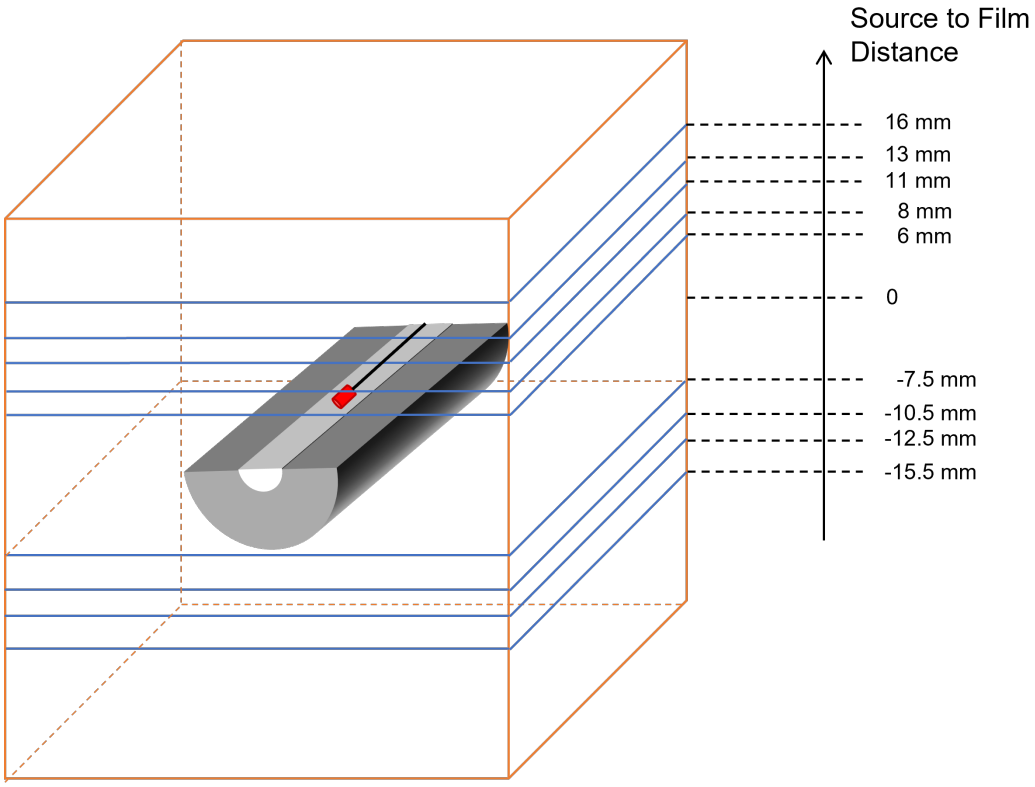

Figure 2.6: Radiochromic film measurement setup. The blue lines represent the positions of the film. The source center to film distance is positive when measured on the unshielded side and negative when measured on the shielded side. Not to scale.

RapidBrachyMCTPS was used to calculate the dose distribution of a water phantom with 10^9 histories and a 1 x 1 x 1 mm^3 scoring grid. The microSelectron Ir-192 HDR v2 source was simulated to match the experiment. The dwell time was set to 1 second and the result was scaled to the appropriate irradiation time. The gamma index method, which is commonly used in intensity-modulated radiation therapy for quality assurance, was performed to determine the agreement between the measured and calculated results. It is defined as:

$$\gamma(\mathbf{r}_m) = min\left\{\Gamma(\mathbf{r}_m, \mathbf{r}_c)\right\} \forall(\mathbf{r}_c), \tag{2.1}$$

where

$$\Gamma(\mathbf{r}_m, \mathbf{r}_c) = \sqrt{\frac{r^2(\mathbf{r}_m, \mathbf{r}_c)}{\Delta d^2} + \frac{\delta^2(\mathbf{r}_m, \mathbf{r}_c)}{\Delta D^2}}, \tag{2.2}$$

$$r(\mathbf{r}_m, \mathbf{r}_c) = |\mathbf{r}_m, \mathbf{r}c|, \tag{2.3}$$

$$\delta(\mathbf{r}_m, \mathbf{r}_c) = D_c(\mathbf{r}_c) - D_m(\mathbf{r}_m) \tag{2.4}$$

Δd is the distance to agreement and ΔD is the dose difference. The passing criterion is $\gamma(\mathbf{r}_m) \leq 1$ (Li et al., 2011). In other words, for a point in the measured dose distribution ($\mathbf{r}_m$), there exists a point in the calculated dose distribution ($\mathbf{r}_c$) within Δd and ΔD. Because the use of the gamma index method for brachytherapy is relatively novel, there exist no standardized criteria for brachytherapy dosimetry.

2.4 Plastic scintillator detector measurements

The depth dose curve shows the absorbed dose at different distances along the beam axis. It was measured in solid water using an independent scintillation dosimetry system (Hyperscint; MedScint Inc., Quebec, Candada). The customized probe had a diameter and length of 1.1 mm and 1.0 mm, respectively. It was encased in a 2.8 mm diameter plastic jacket and coupled with a 20 m long clear optical fiber to guide the light towards a

photodetector. The microSelectron Ir-192 HDR v2 source was used with a single dwell position at the center of the shield. The system was calibrated at 3 mm from the source on the unshielded side with a dwell time of 30 seconds. Cerenkov stem signal was removed using the spectral method (Therriault-Proulx et al., 2012). First, the pure scintillation spectrum was determined by isolating the sensitive volume of the detector in the radiation field with a lead collimator (Figure 2.7a). Measurements with the optic fiber inside and outside the beam were then performed (Figures 2.7b and 2.7c) and the difference between the two, which corresponds to the cerenkov spectrum, was computed.

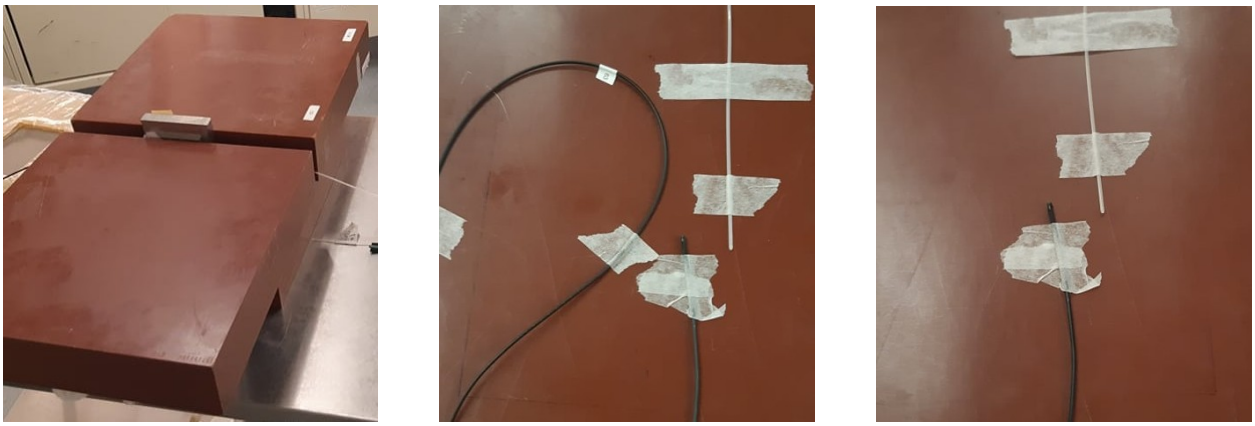

(a) **(b)** **(c)**

Figure 2.7: Spectral method setup to remove cerenkov stem signal. a) Pure scintillation spectrum measurement. Measurement with the optic fiber (b) in and (c) out of the radiation beam.

After the scintillator was calibrated, the shield was placed on a block of solid water with the shielded side facing up. A 3 mm slab of solid water was placed on top and the detector was aligned with the chosen dwell position. Bolus was used to fill any air gaps around the shield. The dwell time was set to 60 seconds to ensure good signal. The measurement was repeated with different thicknesses of solid water as shown in Figure 2.8. The depth dose curve was also determined on the unshielded side using the same setup. The source to detector distance is calculated as follows: distance from the center of the

source to the edge of the shield (1 mm on the unshielded side and 7.5 mm on the shielded side) + thickness of solid water + radius of the scintillator casing (1.4 mm). Results were compared with MC-generated dose depth curves using the same dose maps as calculated previously for radiochromic film measurements.

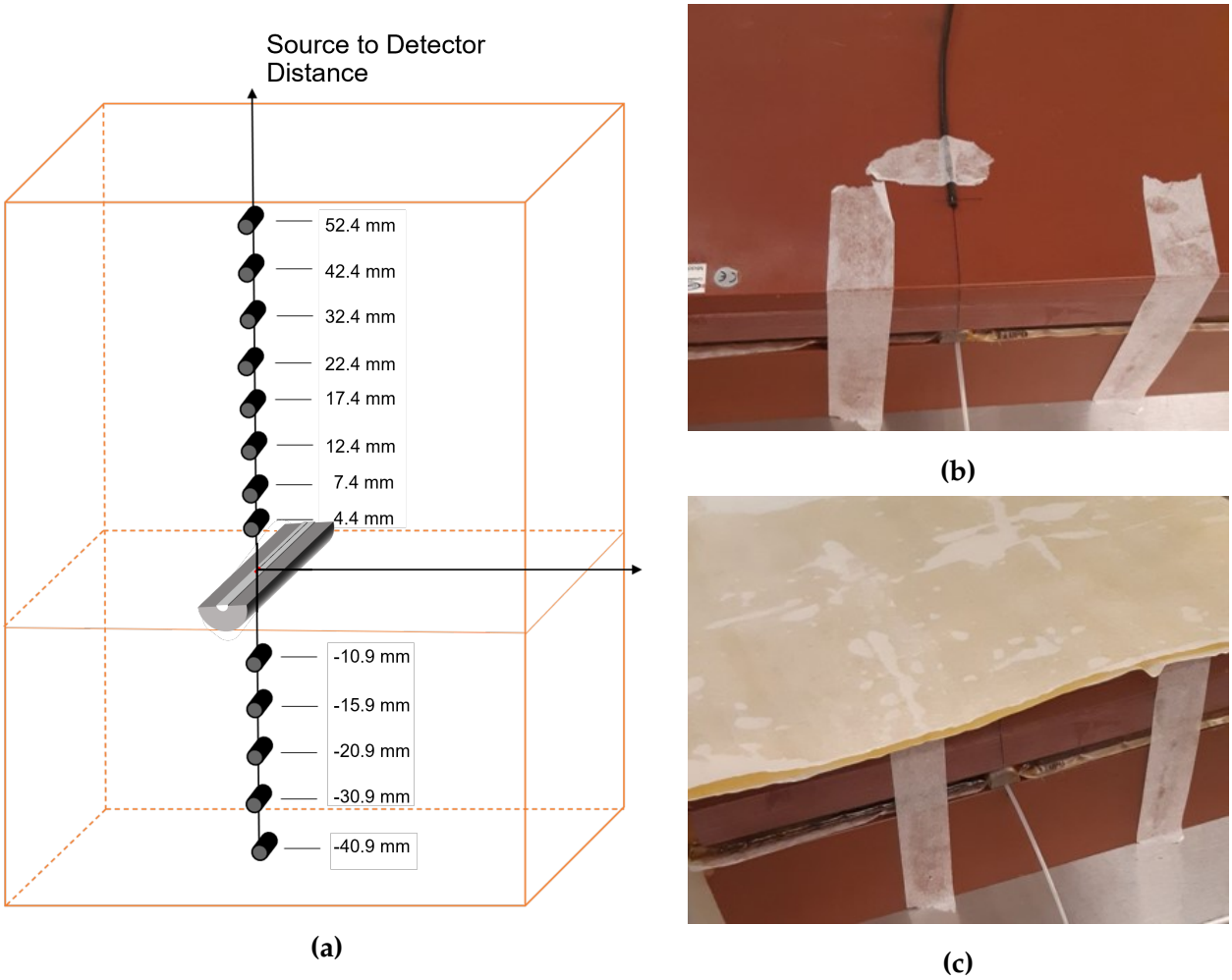

Figure 2.8: Scintillator detector measurement setup. (a) The source center to detector center distance is positive when measured on the unshielded side and negative when measured on the shielded side. Not to scale. (b) The detector was aligned with the source and (c) 1 cm of bolus was used to replicate full scatter conditions.

Chapter 3

Results

3.1 Dynamically-rotating IMBT shield design

Treatment plans created with the initial 2 mm emission window shield design showed total treatment times approaching 60 minutes in certain cases, which is not realistic in a clinical setting. Indeed, patients are often elderly and can have difficulty lying motionless for extended periods of time. Plans generated with the 18 mm diameter shield resulted in an average increase of the treatment time of over 3 minutes. Thus, both models had to be rejected and alternative designs were investigated until an acceptable treatment time was obtained for all patients. This time was defined as less than 30 minutes according to recommendations by Dr. Té Vuong, a radiation oncologist working in close collaboration on the project. Finally, the 180° emission window design was chosen.

3.2 Monte Carlo simulations

Tumor dimensions for patients included in this study are presented in Table 3.1. Although all patients had nonobstructing semicircumferential tumors, we can observe that the CTVs vary greatly in volume and length. For this reason, it is important to design a shield that can be used for a wide range of target dimensions. Additionally, the de-

livery times obtained from MC-based treatment plans with no shielding, static shielding and dynamic shielding are listed. On average, the treatment time increased by a factor of 2.21 and 2.16 when dynamic shielding was used compared with no shielding and static shielding, respectively. Unsurprisingly, similar treatment times are obtained with both HDREBT techniques as the static shield does not affect the dose distribution on the side of the target.

Patient	Fraction	CTV volume (cc)	CTV length (mm)	Treatment time (min)		
				No Shielding	Static Shielding	Dynamic Shielding
1	1	13.91	33	8.12	8.10	20.14
	2	7.69	24	7.35	8.02	19.04
	3	19.69	48	10.79	11.00	26.61
2	1	5.10	39	4.67	4.93	12.35
	2	3.82	21	4.58	4.57	10.22
	3	1.98	21	3.51	3.74	8.66
3	1	6.07	21	5.45	5.44	13.94
	2	9.58	27	7.54	7.58	15.61
	3	7.54	21	6.07	6.14	15.82
4	1	11.62	33	8.95	9.08	13.67
	2	9.32	30	6.36	6.49	10.53
	3	12.23	27	8.78	8.82	14.84
Mean $\pm$ SD		9.04 ± 4.86	25.75 ± 8.43	6.85 ± 2.13	6.99 ± 2.14	15.12 ± 4.97

Table 3.1: Tumor dimensions and total treatment times obtained with three shielding methods (no shielding, static shielding and dynamic shielding).

The optimized dose distributions for an example patient treated with the conventional endorectal applicator and dynamically-rotating shield are shown in Figure 3.1. The isodose lines were least conformal to the target contour (in red) when no shielding was used and most conformal when dynamic shielding IMBT was used. This is further supported by the results of the DVH analysis presented below. The 100% isodose line corresponds to the prescribed dose, while the 200% isodose line can indicate the presence of hot spots.

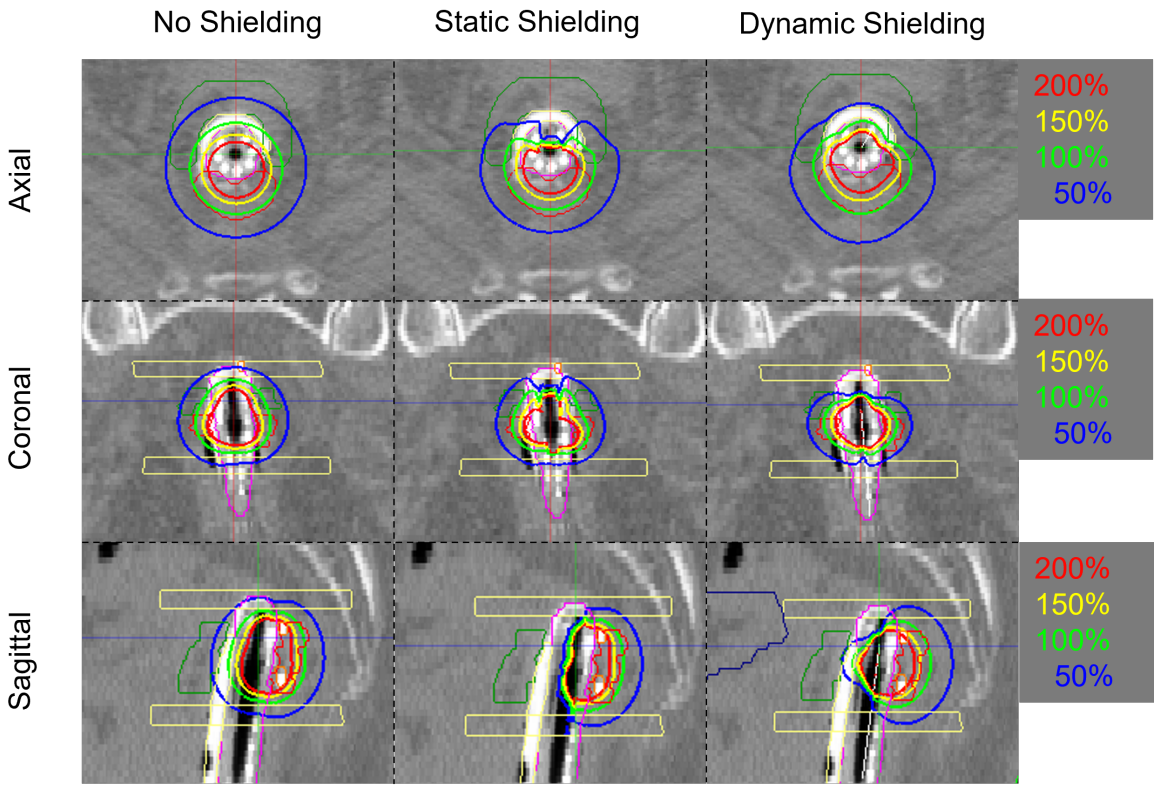

Figure 3.1: Optimized dose distributions (CTV $D_{90\%}$ = 10 Gy) obtained with the three shielding methods. The 100% isodose line is in green. The CTV is contoured in red, the contralateral healthy rectal wall in green, the superior and inferior dose spill regions in yellow and the applicator in magenta.

DVH metrics were computed for the target and different OARs to permit plan evaluation. Table 3.2 presents a summary of these results. Statistically significant values are shown in bold (P-value < 0.05). In addition to providing significantly higher CTV coverage, the dynamic shield also resulted in better sparing of the contralateral healthy rectal wall, rectum, bladder, femur and pelvis compared to the conventional applicator with and without static shielding. However, the leakage to the inferior dose spill region was significantly higher when compared to the static shielding method due to the greater total treatment time. The superior dose spill region also received more dose, although this increase was not statistically significant. Figures 3.2 and 3.3 show box and whisker plot comparisons of the three different treatment modalities.

Structure \ Type of Shielding	Dynamic Shielding	No Shielding	P-value	Static Shielding	P-value
CTV $D_{90\%}$ (Gy)	10.02 ± 0.03	9.90 ± 0.06	$<$ **0.01**	9.95 ± 0.08	**0.01**
Contralateral D_{2cc} (Gy)	4.43 ± 0.94	7.48 ± 1.44	$<$ **0.01**	6.91 ± 1.44	$<$ **0.01**
Superior D_{2cc} (Gy)	4.62 ± 1.18	4.32 ± 1.22	0.06	4.25 ± 1.28	0.06
Inferior D_{2cc} (Gy)	5.27 ± 1.02	5.04 ± 1.02	0.24	4.74 ± 0.89	$<$ **0.01**
Rectum $D_{50\%}$ (Gy)	1.19 ± 1.02	2.64 ± 1.83	$<$ **0.01**	1.65 ± 1.18	$<$ **0.01**
Bladder $D_{50\%}$ (Gy)	0.37 ± 0.14	0.68 ± 0.26	$<$ **0.01**	0.44 ± 0.12	**0.04**
Femur $D_{50\%}$ (Gy)	0.13 ± 0.03	0.18 ± 0.06	$<$ **0.01**	0.15 ± 0.04	**0.04**
Pelvis $D_{50\%}$ (Gy)	0.29 ± 0.08	0.42 ± 0.14	$<$ **0.01**	0.35 ± 0.12	$<$ **0.01**

Table 3.2: DVH metrics. Results are presented as mean $\pm$ SD. P-values are calculated relative to "Dynamic Shielding". Statistically significant differences are in bold.

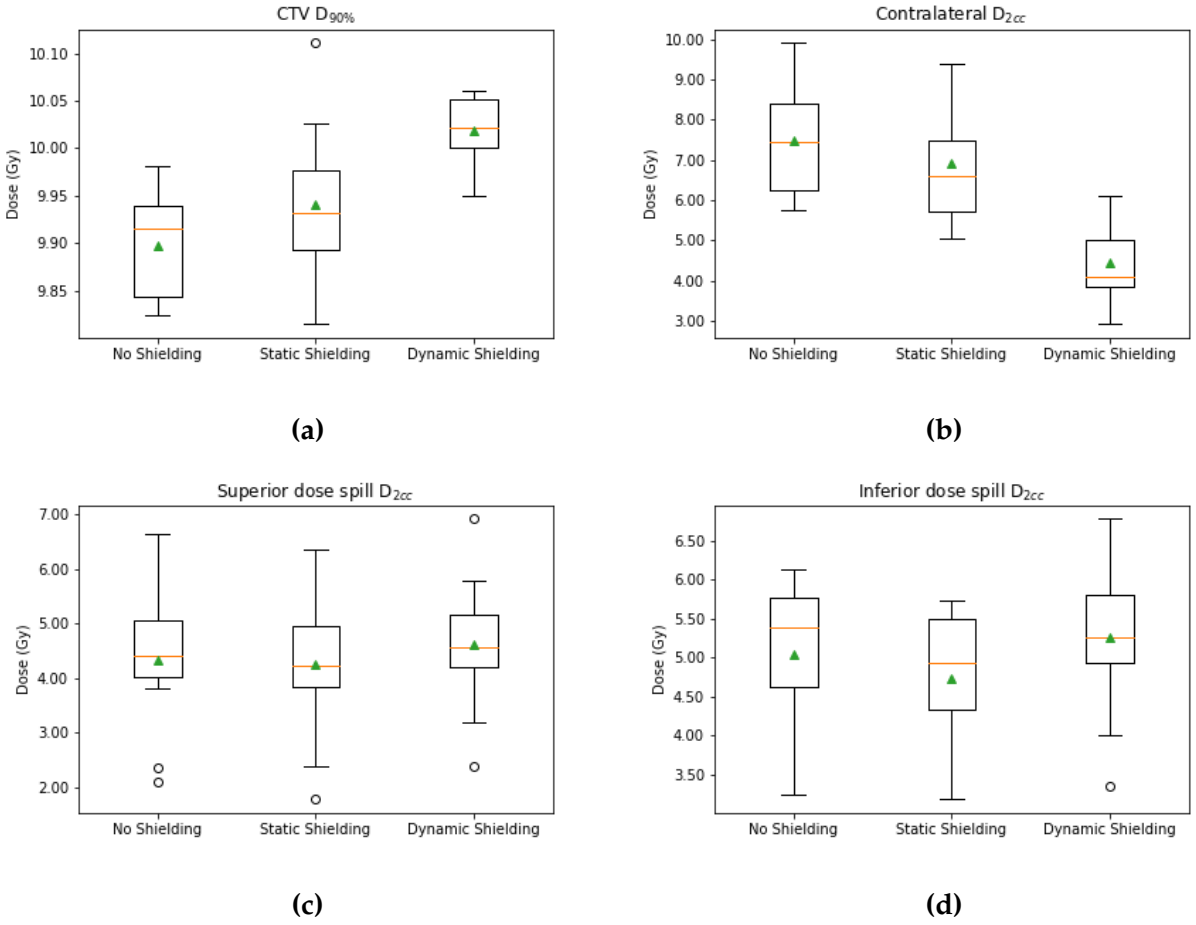

Figure 3.2: Delivery method comparison (conventional applicator with and without static shielding and dynamically-rotating IMBT shield) calculated with a generic Ir-192 source. (a) Clinical target volume $D_{90\%}$, (b) contralateral rectum wall D_{2cc}, (c) superior dose spill region D_{2cc} and (d) inferior dose spill region D_{2cc}. The orange line shows the median. Whiskers indicate the maximum and minimum excluding outliers which are shown as points. The green triangle shows the mean.

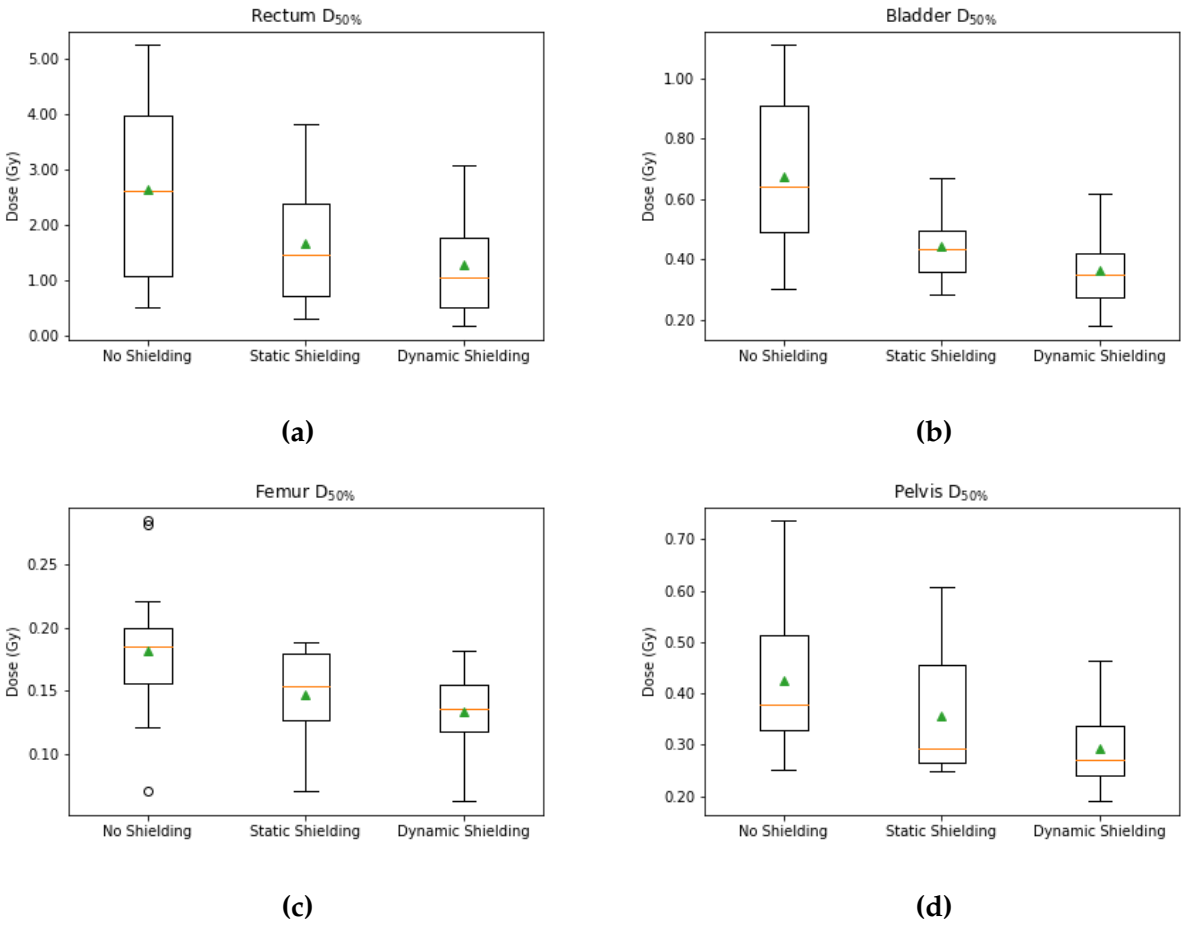

Figure 3.3: Delivery method comparison (conventional applicator with and without static shielding and dynamically-rotating IMBT shield) calculated with a generic Ir-192 source. (a) Healthy rectum $D_{50\%}$, (b) bladder $D_{50\%}$, (c) femur $D_{50\%}$ and (d) pelvis $D_{50\%}$. The orange line shows the median. Whiskers indicate the maximum and minimum excluding outliers which are shown as points. The green triangle shows the mean.

Dose homogeneity in the CTV, defined as the ratio of the volume receiving at least 200% of the prescribed dose to the volume receiving at least 100% of the prescribed dose, was calculated for all cases (Morcos and Enger, 2020). These results are presented in Figure 3.4. Smaller values of this ratio indicate fewer hot spots in the structure. On average, dynamic shielding IMBT leads to a more homogeneous dose distribution compared with no shielding and static shielding (P-value = 0.03 and 0.04, respectively). Results were not statistically different between both methods using the conventional applicator (P-value = 0.89).

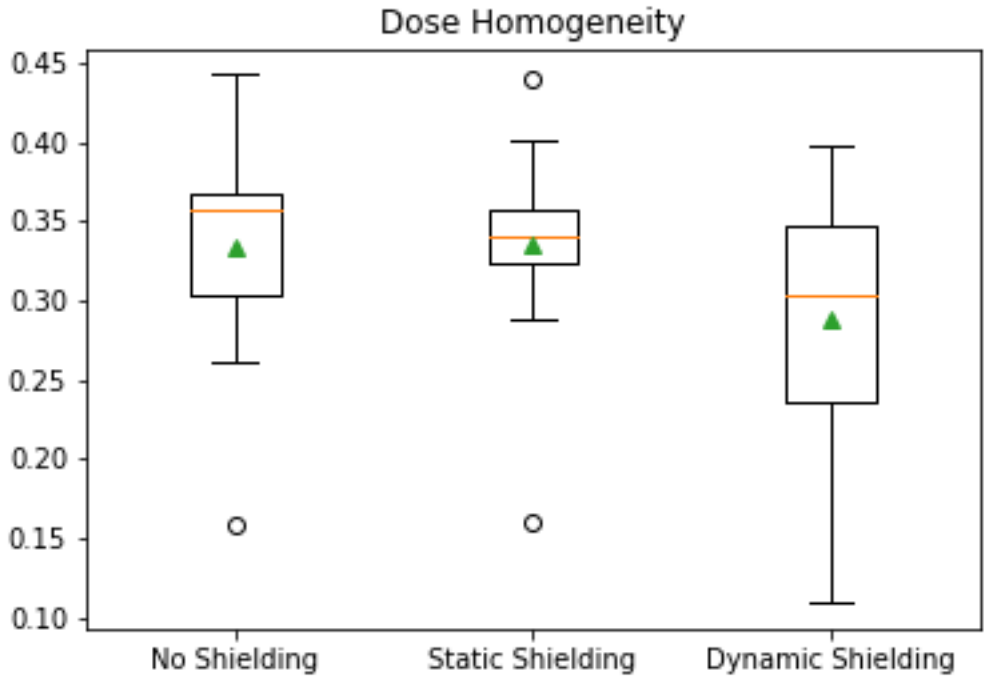

Figure 3.4: Dose homogeneity in the CTV defined as $\frac{V_{200\%}}{V_{100\%}}$ calculated for three shielding methods. The orange line shows the median. Whiskers indicate the maximum and minimum excluding outliers which are shown as points. The green triangle shows the mean.

3.3 Radiochromic film measurements

The dose distribution at different distances from the source was measured with radiochromic film in solid water. Results were compared with MC-generated dose maps, and agreement was evaluated by computing the absolute dose difference as well as the gamma index with a distance to agreement of 2 mm and a percent dose difference of 2%. This choice of criteria was based on recommendations by Yang and Rivard (Yang and Rivard, 2011). Figures 3.5 and 3.6 show the measured and calculated dose colorwash at multiple distances from the source on the shielded side and unshielded side, respectively. The absolute dose difference and gamma index maps are also presented. The gamma index pass rate was greater than 95% in all cases. In general, gamma index values greater than one were concentrated in the center of the image, which coincides with regions of bigger absolute dose differences. This is in concordance with what Yang and Rivard observed: "failure regions were located within the brachytherapy source, near the brachytherapy source surface, or in high dose-gradient regions" (Yang and Rivard, 2011). The biggest absolute dose difference was measured 7.5 mm away from the source on the shielded side. In this case, the film was placed directly on the surface of the shield. However, in a clinical setting, the shield would be encased in a silicone sleeve and a contralateral balloon would be used such that the OARs are further away from the source where we measure smaller absolute dose differences and a better gamma index passing rate. In Figure 3.6, we can observe a red-blue pattern in the absolute dose difference map for multiple distances to the source which can be due to errors in alignment between the two dose distributions. However, this is partly taken into account by the distance to agreement in the gamma index analysis. According to the manufacturer, solid water mimics true water within 0.5%. Thus, a Type B uncertainty of 0.5% was added to all measurements performed with this material and compared to MC simulations in water.

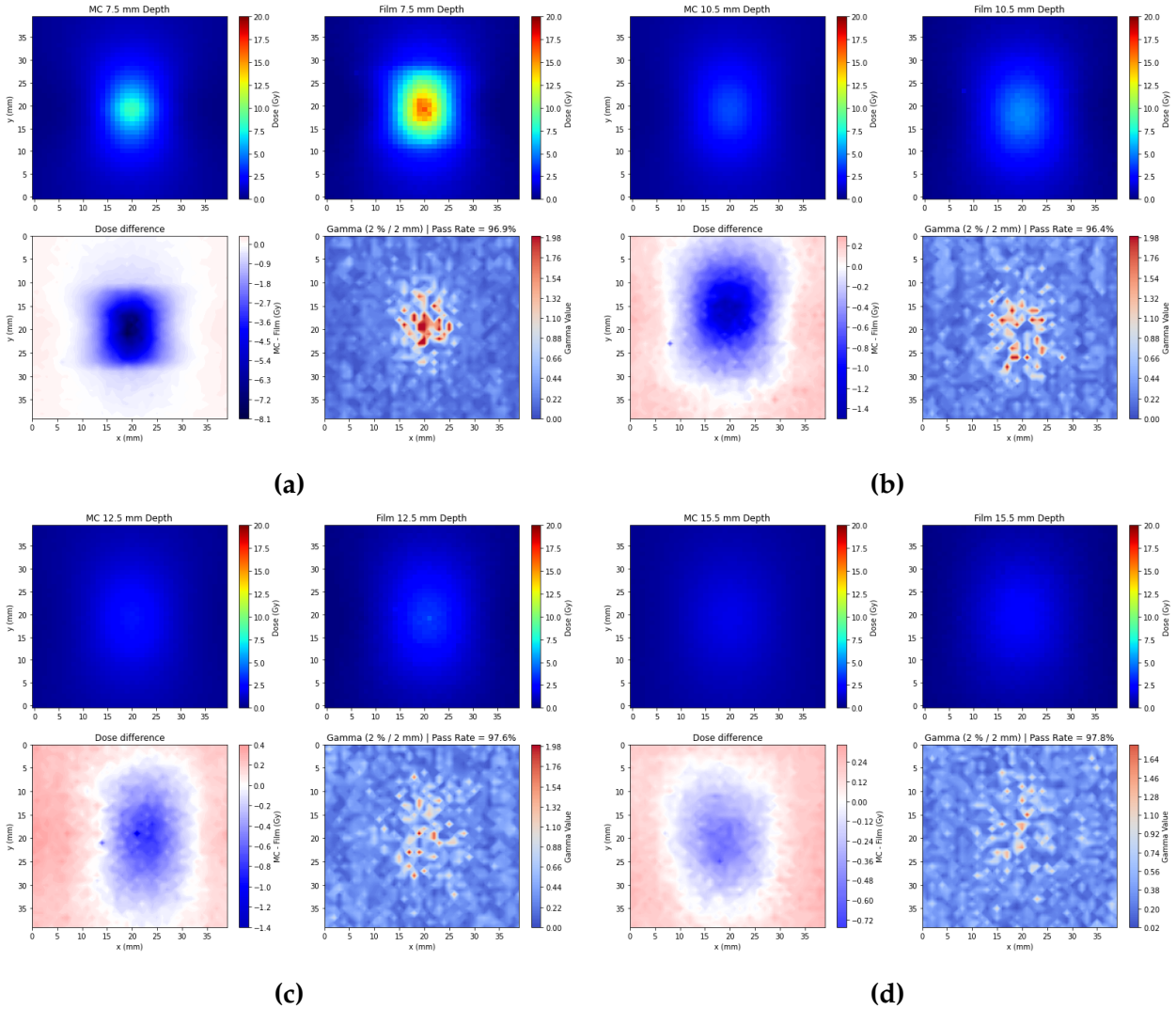

Figure 3.5: Dose distribution on the shielded side calculated with MC and measured with radiochromic film at (a) 7.5 mm, (b) 10.5 mm, (c) 12.5 mm and (d) 15.5 mm from the source. The dwell time was set to 400 seconds. The absolute dose difference and gamma value are shown.

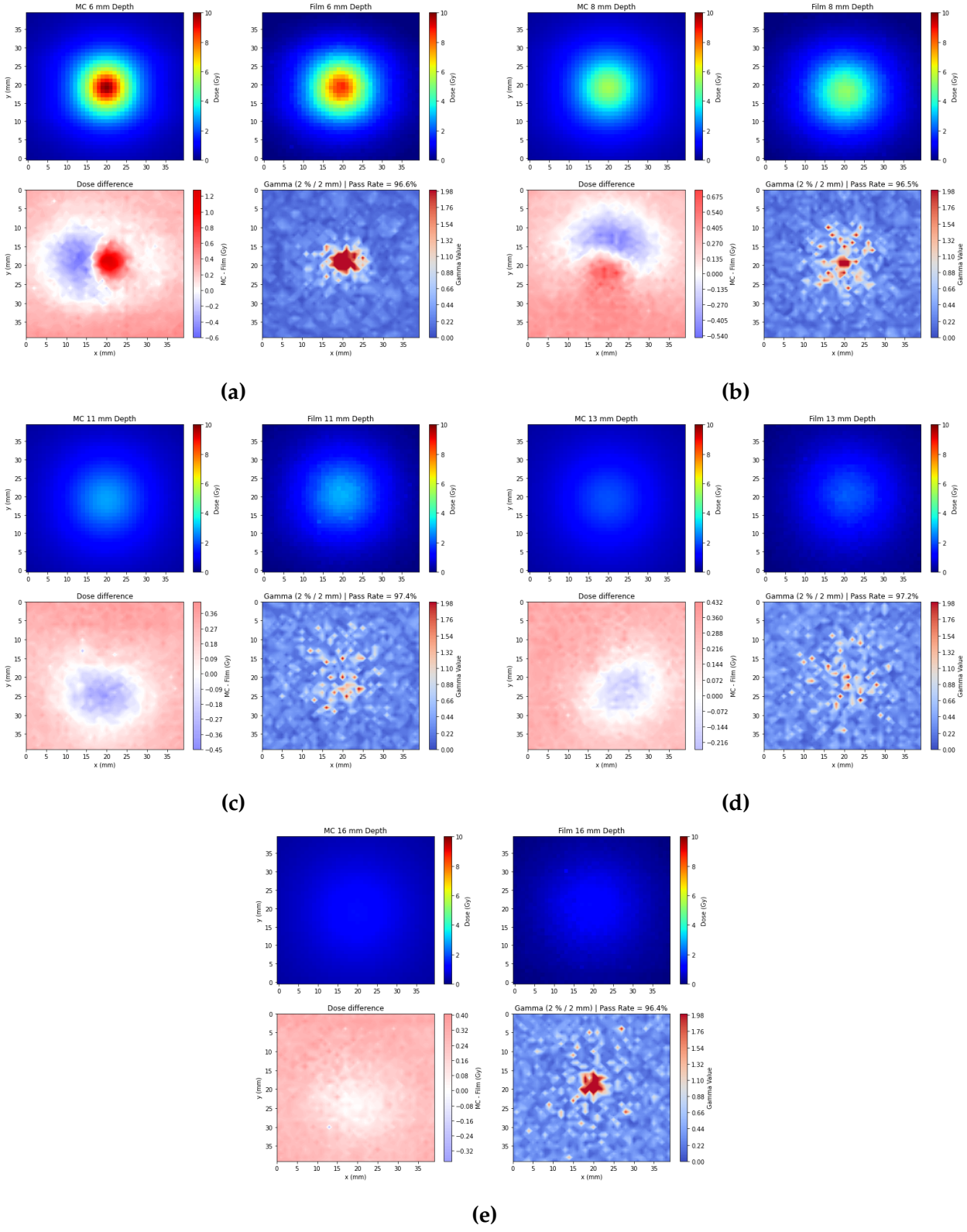

Figure 3.6: Dose distribution on the unshielded side calculated with MC and measured with radiochromic film at (a) 6 mm, (b) 8 mm, (c) 11 mm, (d) 13 mm and (d) 16 mm from the source. The dwell time was set to 45 seconds. The absolute dose difference and gamma value are shown.

3.4 Plastic scintillator detector measurements

Figure 3.7 compares the relative dose at different distances from the source measured with a scintillator detector and calculated with MC on the shielded and unshielded sides (the shield is illustrated in gray and the source is in magenta). The dose was normalized to the value measured at 12.4 mm from the source on the unshielded side. The scintillating probe measured the dose rate at every second for one minute. The dose for one second was taken as the mean, while the error corresponded to the standard deviation (excluding the build-up and build-down regions). The uncertainty on the source to detector distance was rounded up to 1 mm. Indeed, up to four blocks of solid water were placed between the shield and detector for each measurement, and each block had an uncertainty of 0.5 mm on its width. The dashed curve shows the MC results for a maximum misalignment of the probe (estimated to be 2 mm in each direction). The Type A uncertainty of MC-generated values was less than 0.05%. The upper graph in Figure 3.7 shows that the shield is very efficient at attenuating the radiation beam as the relative dose values on the shielded side are significantly lower. The figure also includes a graph of the percent difference, which is generally higher (in absolute value) on the shielded side as well as for greater distances from the source because the doses are very small. We also observe that the measured dose is smaller than the calculated value closer to the source, while the opposite is true as we move further away.

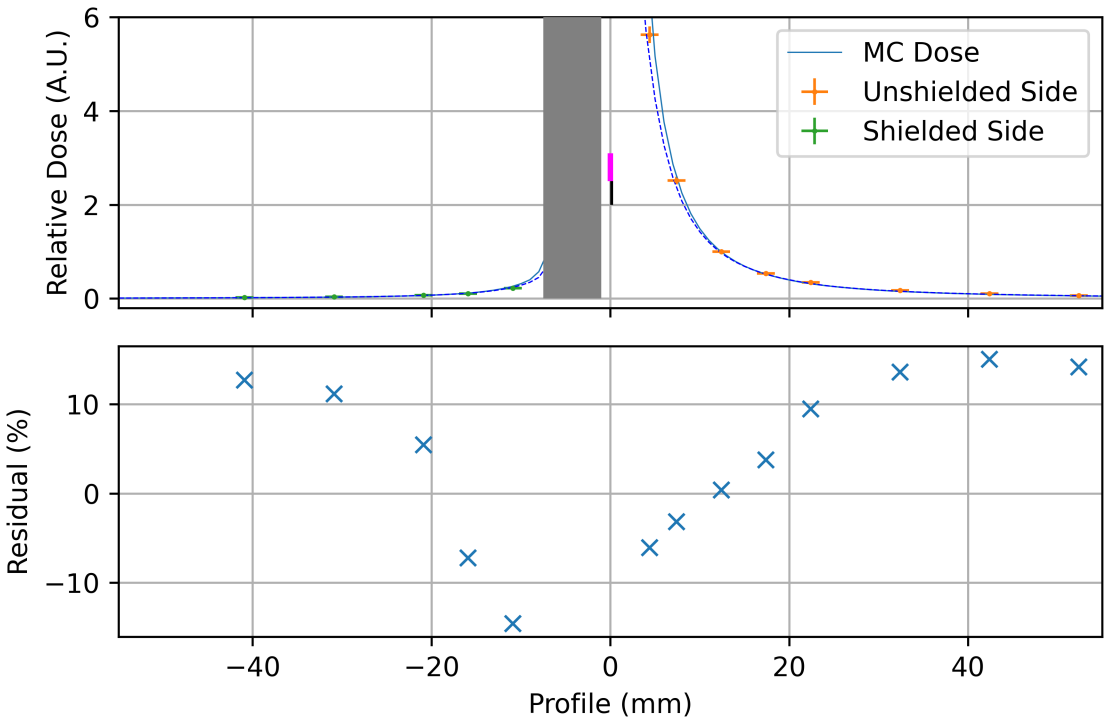

Figure 3.7: Depth dose curve calculated with MC and measured with a scintillator detector (top), and percent difference between both values (bottom).

Chapter 4

Discussion

In this work, the dosimetric impact of replacing the intracavitary mold applicator with an MRI-compatible rotating shield was studied. MC simulations were performed to calculate and compare the dose distributions produced by each treatment modality. Experimental measurements validated the dose calculation algorithm and demonstrated the safety of the new system.

4.1 Monte Carlo simulations

Endorectal HDR brachytherapy treatment plans were generated using MC for three devices: ICMA with no shield, ICMA with static shield and dynamically-rotating IMBT shield. Results show significant dosimetric gains when using the latter as the contralateral wall, rectum, bladder, femur and pelvis all received less dose. Yet, the inferior and superior dose spill regions received more dose compared with the static shielding method. The clinical significance of this increase is unclear and needs to be investigated. In this work, the dynamically-rotating shield was encapsulated in a 2.5 mm thick water-equivalent sheath so that the total diameter of the applicator matched the diameter of the ICMA present in pre-treatment CT images. However, in practice, a thinner sheath (1 mm) could be used. Consequently, the source would be closer to the target which would

decrease the treatment time and dose spillage. Therefore, the dose to the OARs obtained with the dynamic shielding method should be taken as an upper limit.

A study by Webster *et al.* investigated 15 single-depth applicators and one dual-depth applicator for the treatment of rectal carcinomas with an Ir-192 source (Webster et al., 2013b). Similar to our work, all applicators were composed of high-density tungsten alloy and MC was used to calculate optimized treatment plans for 13 patients (36 fractions). However, contrary to our design, the applicators remained immobile once inserted inside the rectum. Authors found that for the same CTV coverage as the conventional ICMA with static shielding, the 12-channel, 1-mm depth, and 14-channel, 2-mm depth designs resulted in improved lateral spill and contralateral healthy rectum doses by over 10% and 30%, respectively. The more complex 10-channel dual-depth design outperformed every single-depth applicators. The same authors also investigated dynamic modulated endorectal brachytherapy (Webster et al., 2013a). Their shield was a 45 mm long tungsten alloy cylinder with a small window on one side to encapsulate an Ir-192 source. The shield could be rotated and translated during treatment using a robotic arm. This extra degree of freedom complicates the delivery and increases the risk of positional errors. For clinical patient cases, a 19 mm diameter shield was compared to the ICMA using MC. They found a 40% decrease of the dose heterogeneity index, defined as $\frac{D_{max}-D_{min}}{D_{mean}}$, and a 40% to 60% reduction of the $D_{98\%}$ of all critical structures evaluated. However, the treatment time increased by a factor of 2.75 on average. The smaller diameter of our shield design makes it more comfortable for patients.

Furthermore, the dose homogeneity ratio in the tumor was significantly lower when using dynamic-shielding. This is clinically relevant as the presence of hot spots is a limiting factor for dose escalation in the target. The use an ipsilateral balloon could further improve dose conformity (Devic et al., 2019). A study investigating IMBT of cervical cancer found a dose homogeneity within 12% fo the conventional tandem for three tungsten

dynamically-rotating shield designs (Morcos and Enger, 2020).

An important limitation of our study is the small number of patients. In the future, a greater number of cases must be planned and a robust statistical analysis must be performed. This will also permit a better understanding of the dose spillage to the superior and inferior regions. We estimate that 20 patients totaling 60 fractions will be needed, but this number still needs to be confirmed.

4.2 Radiochromic film measurements

Radiochromic film measurements were performed in solid water with a prototype of the dynamic shield design and an Ir-192 source. Gamma index analysis was carried out to determine the agreement between the measured and MC-calculated dose distributions. The gamma index pass rate was greater than 95% for all fractions, which validated our dose calculation algorithm. However, some differences can be seen, mostly in the central region. The presence of air gaps in the setup can partly explain why the measured dose on the shielded side was higher because air does not attenuate the radiation beam as much as solid water. This could be corrected in the future by drilling a fitted hole in the block of solid water for the insertion of the shield. The unshielded side had a flat edge which made air gaps less likely. This might explain why the dose differences are smaller on this side. Overall, agreement between measured and MC-calculated dose maps were considered good taking into account registration uncertainties of a few millimeters.

4.3 Plastic scintillator detector measurements

The depth dose curve was measured with a scintillator detector in solid water and calculated with MC to illustrate the attenuating capacity of the dynamic shield design. Al-

though the absolute difference between both values was relatively small, the percent difference reached approximately 15% at certain distances. For results closer to the source, this can be explained by the significant positional uncertainties associated with the setup. The scintillator was visually aligned with the chosen dwell position which introduced important human error. We can see that if this taken into account (dashed line), then the measured value agrees with MC. For results further than 10 mm, the measured dose is systematically greater than the calculated one. This overresponse follows a smooth trend, which indicates that it is probably due to the energy dependence of the detector. Indeed, the beam hardens as it travels through the material and interacts differently with the probe. This should be corrected for in future experiments. Another study using scintillator detectors built by Medscint found dose differences between scintillator measurements in water and TPS calculations within 1% (Cloutier, Beaulieu, and Archambault, 2021). By building a specialized holder for our experiment and optimizing the probe design to our specific needs, we hope to obtain similar differences in the future. Nevertheless, initial results show a significant decrease of the dose on the shielded side (Figure 3.7).

4.4 Future work for clinical translation

4.4.1 Dynamically-rotating IMBT shield design

To permit easy insertion inside the rectal lumen, future iterations of our dynamically-rotating shield must have a certain flexibility. Indeed, after about the first 10 cm, the rectum bends quite sharply in some cases. Therefore, a rigid tungsten shield is not conceivable as it could cause great discomfort and pain to the patient, and even puncture the organ. The "chess-piece" model has been proposed as a solution. It is made of individual bell-shaped components that are stacked together as shown in Figure 4.1. Half of the shield would be made of tungsten and the other half of plastic to permit an 180° emission window. The next steps of this project are to model this design and create MC-based treatment plans to evaluate its rectum sparing capacity compared with the conventional

applicator. In particular, the dose leakage at the joints between the separate components need to be calculated.

Another shield design option it to keep the "chess-piece" idea, but decenter the catheter channel so that the source is closer to the tumor. This way, the treatment time could be decreased which would facilitate the transition of our technology to the clinic. In fact, an important advantage of the conventional applicator over our current design is that the source is placed in circumferential catheter channels and is therefore closer to the target. The gain in treatment time would have to be calculated with MC. If this design is chosen, the rotating delivery system would have to be modified to avoid kinks in the catheter.

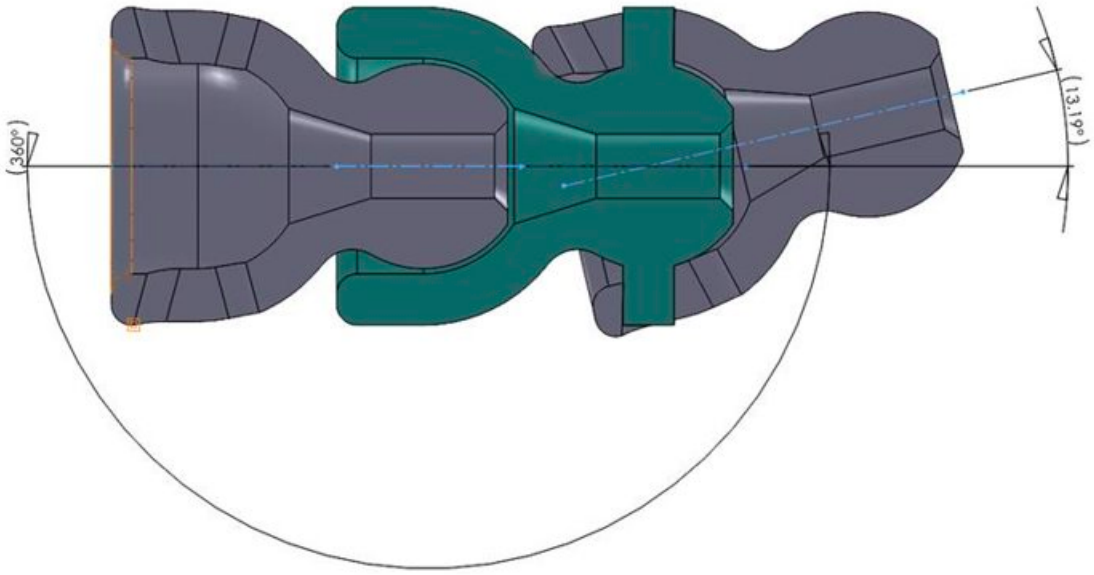

Figure 4.1: "Chess-piece" design of dynamically-rotating shield.

4.4.2 Treatment delivery

The rotating delivery system developed previously in our lab for prostate IMBT will need to be adapted to the new shield design. Software will then be written to connect the delivery system to the TPS. Moreover, alternative source radioisotopes will be investigated, and treatment plans optimized for dosimetry investigations. The goal is to find the source and applicator design combination that delivers the best dose distribution inside the tumor, while minimizing the dose to the OARs. Previous studies have found that IMBT with Yb-169 for the treatment of cervical and prostate cancers leads to improved tumor coverage and OAR sparing compared with IMBT using an Ir-192 source (Morcos et al., 2021; Famulari, Duclos, and Enger, 2020).

4.4.3 Plastic scintillator detector measurements

As mentioned previously, a specially designed holder must be made for scintillator measurements in water in order to reduce the positional uncertainties. An initial model is shown in Figure 4.2. The central hole is 2 mm in diameter to permit the insertion of a 6F catheter, while all other holes have a 3 mm diameter to accommodate the detector. The shield will be placed in the center and held in place by four nylon screws extending radially from the support poles. To measure the depth dose curve, the scintillating probe will be successively placed in each hole along a chosen axis. Additionally, measurements must be performed to determine the anisotropy of the shield. Finally, the goal is to introduce comprehensive quality assurance tests based on scintillator detector technology that will be performed in the clinic to ensure the safety of our system.

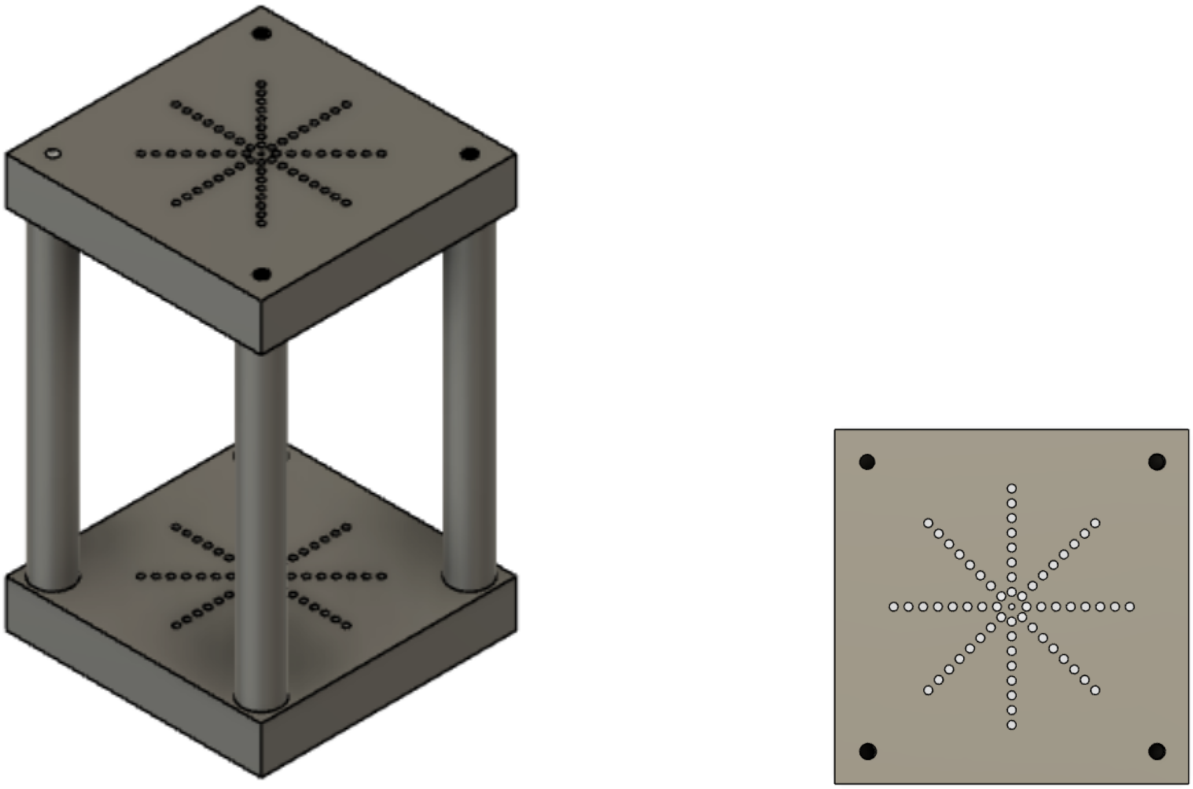

(a) **(b)**

Figure 4.2: Initial design of a holder for scintillator detector measurements in water. (a) Full view. (b) Top view.

Chapter 5

Conclusion

In this work, we presented a novel MRI-compatible dynamic shielding IMBT applicator for the treatment of rectal cancer. We optimized treatment plans using a research MC-based TPS to show that this method permits dose escalation inside the tumor while more effectively shielding the OARs compared to conventional HDREBT. Experimental measurements with radiochromic film in solid water validated our dose calculation algorithm and demonstrated the safety of our system by showing the attenuation properties of the shield. Finally, relative dose measurements at different depths with a scintillator detector showed that the shield is very effective at blocking the radiation beam, even though difference with MC simulations were relatively large.

Future versions of the dynamically-rotating shield will be flexible to permit easy insertion inside the rectum. Also, the robustness of the delivery system developed at our lab for IMBT of prostate cancer will be tested and validated. Additional scintillator measurements will be performed with a specialized holder to determine the percent depth dose curve as well as the anisotropy of our shield.

Dose escalation inside the tumor while simultaneously reducing toxicity will significantly improve the potential of HDR-BT. This will also increase the quality of life of patients and lead to improved therapeutic ratio and clinical outcomes.

Bibliography

Aldelaijan, Saad et al. (2011). "Radiochromic film dosimetry of HDR 192Ir source radiation fields". In: *Medical physics* 38.11, pp. 6074–6083.

Antaki, Majd, Christopher L Deufel, and Shirin A Enger (2020). "Fast mixed integer optimization (FMIO) for high dose rate brachytherapy". In: *Physics in Medicine & Biology* 65.21, p. 215005.

Beaulieu, Luc et al. (2012). "Report of the Task Group 186 on model-based dose calculation methods in brachytherapy beyond the TG-43 formalism: current status and recommendations for clinical implementation". In: *Medical physics* 39.10, pp. 6208–6236.

Beddar, Sam et al. (2021). "Recent Advances and Clinical Applications of Plastic Scintillators in the Field of Radiation Therapy". In: *Plastic Scintillators*. Springer, pp. 425–460.

Bekerat, Hamed et al. (2014). "Improving the energy response of external beam therapy (EBT) GafChromicTM dosimetry films at low energies (100 keV)". In: *Medical physics* 41.2, p. 022101.

Bethesda, M (1992). *Icru report n. 46: Photon, electron, proton and neutron interaction data for body tissues*. Tech. rep. Tech. Rep.

Brenner, Darren R et al. (2020). "Projected estimates of cancer in Canada in 2020". In: *Cmaj* 192.9, E199–E205.

Callaghan, Cameron M et al. (2019). "Systematic review of intensity-modulated brachytherapy (IMBT): static and dynamic techniques". In: *International Journal of Radiation Oncology* Biology* Physics* 105.1, pp. 206–221.

Chargari, Cyrus et al. (2019). "Brachytherapy: An overview for clinicians". In: *CA: a cancer journal for clinicians* 69.5, pp. 386–401.

Chassagne, D. et al. (Apr. 2016). "Report 38". In: *Journal of the International Commission on Radiation Units and Measurements* os20.1, NP–NP. ISSN: 1473-6691. DOI: 10.1093/jicru/os20.1.Report38. eprint: https://academic.oup.com/jicru/article-pdf/os20/1/NP/9586787/jicruos20-NP.pdf. URL: https://doi.org/10.1093/jicru/os20.1.Report38.

Cloutier, Emily, Luc Beaulieu, and Louis Archambault (2021). "Deformable Scintillation Dosimeter II: Real-Time Simultaneous Measurements of Dose and Tracking of Deformation Vector Fields". In: *arXiv preprint arXiv:2101.08835*.

Devic, Slobodan, Nada Tomic, and David Lewis (2016). "Reference radiochromic film dosimetry: review of technical aspects". In: *Physica Medica* 32.4, pp. 541–556.

Devic, Slobodan et al. (2019). "Optimization of HDRBT boost dose delivery for patients with rectal cancer". In: *Brachytherapy* 18.4, pp. 559–563.

Ebert, MA (2002). "Possibilities for intensity-modulated brachytherapy: technical limitations on the use of non-isotropic sources". In: *Physics in Medicine & Biology* 47.14, p. 2495.

Enger, Shirin A et al. (2012). "Layered mass geometry: a novel technique to overlay seeds and applicators onto patient geometry in Geant4 brachytherapy simulations". In: *Physics in Medicine & Biology* 57.19, p. 6269.

Famulari, G and S A Enger (2018). "OC-0173: Intensity modulated brachytherapy system for dynamic modulation of shielded catheters". In: *Radiotherapy and Oncology* 127, S90. ISSN: 0167-8140. DOI: https://doi.org/10.1016/S0167-8140(18)30483-3. URL: https://www.sciencedirect.com/science/article/pii/S0167814018304833.

Famulari, Gabriel, Marie Duclos, and Shirin A Enger (2020). "A novel 169Yb-based dynamic-shield intensity modulated brachytherapy delivery system for prostate cancer". In: *Medical physics* 47.3, pp. 859–868.

Famulari, Gabriel et al. (2018). "RapidBrachyMCTPS: a Monte Carlo-based treatment planning system for brachytherapy applications". In: *Physics in Medicine & Biology* 63.17, p. 175007.

Glickman, Harry et al. (2020). "RapidBrachyMCTPS 2.0: A comprehensive and flexible Monte Carlo-based treatment planning system for brachytherapy applications". In: *arXiv preprint arXiv:2007.02902*.

Hannoun-Levi, JM (2017). "11. Disappearing of pulsed-dose rate brachytherapy in favor to high-dose rate: Counterpart debate". In: *Physica Medica: European Journal of Medical Physics* 44, p. 6.

Lewis, David et al. (2012). "An efficient protocol for radiochromic film dosimetry combining calibration and measurement in a single scan". In: *Medical physics* 39.10, pp. 6339–6350.

Li, Heng et al. (2011). "Toward a better understanding of the gamma index: Investigation of parameters with a surface-based distance method a". In: *Medical physics* 38.12, pp. 6730–6741.

Morcos, Marc and Shirin A Enger (2020). "Monte Carlo dosimetry study of novel rotating MRI-compatible shielded tandems for intensity modulated cervix brachytherapy". In: *Physica Medica* 71, pp. 178–184.

Morcos, Marc et al. (2021). "A novel minimally invasive dynamic-shield, intensity-modulated brachytherapy system for the treatment of cervical cancer". In: *Medical physics* 48.1, pp. 71–79.

Morton, GC and PJ Hoskin (2013). "Brachytherapy: current status and future strategies—can high dose rate replace low dose rate and external beam radiotherapy?" In: *Clinical Oncology* 25.8, pp. 474–482.

Nath, Ravinder et al. (1995). "Dosimetry of interstitial brachytherapy sources: recommendations of the AAPM Radiation Therapy Committee Task Group No. 43". In: *Medical physics* 22.2, pp. 209–234.

Nout, RA et al. (2016). "CT-based adaptive high-dose-rate endorectal brachytherapy in the preoperative treatment of locally advanced rectal cancer: Technical and practical aspects". In: *Brachytherapy* 15.4, pp. 477–484.

Podgorsak, Ervin B et al. (2005). *Radiation oncology physics.* IAEA Vienna.

Poon, Emily et al. (2006). "Dosimetric characterization of a novel intracavitary mold applicator for high dose rate endorectal brachytherapy treatment". In: *Medical physics* 33.12, pp. 4515–4526.

Poon, Emily et al. (2008). "Patient-specific Monte Carlo dose calculations for high-dose-rate endorectal brachytherapy with shielded intracavitary applicator". In: *International Journal of Radiation Oncology* Biology* Physics* 72.4, pp. 1259–1266.

Rivard, Mark J et al. (2004). "Update of AAPM Task Group No. 43 Report: A revised AAPM protocol for brachytherapy dose calculations". In: *Medical physics* 31.3, pp. 633–674.

Safigholi, Habib et al. (2018). "Direction modulated brachytherapy (DMBT) tandem applicator for cervical cancer treatment: Choosing the optimal shielding material". In: *Medical physics* 45.8, pp. 3524–3533.

Sempau, J et al. (2001). "Monte Carlo simulation of electron beams from an accelerator head using PENELOPE". In: *Physics in Medicine & Biology* 46.4, p. 1163.

Shoemaker, Tristan et al. (2019). "Dosimetric considerations for ytterbium-169, selenium-75, and iridium-192 radioisotopes in high-dose-rate endorectal brachytherapy". In: *International Journal of Radiation Oncology* Biology* Physics* 105.4, pp. 875–883.

Tamas, K et al. (2015). "Rectal and colon cancer: Not just a different anatomic site". In: *Cancer treatment reviews* 41.8, pp. 671–679.

Therriault-Proulx, François et al. (2012). "Development of a novel multi-point plastic scintillation detector with a single optical transmission line for radiation dose measurement". In: *Physics in Medicine & Biology* 57.21, p. 7147.

Victor, L (2015). "The Difference Between a Collapsed Cone Based and a Monte Carlo Based Dose Calculation Algorithm". In: *RaySearch Laboratories. Stockholm, Sweden*.

Visser, Andries G, GJ Van den Aardweg, and Peter C Levendag (1996). "Pulsed dose rate and fractionated high dose rate brachytherapy: Choice of brachytherapy schedules to replace low dose rate treatments." In: *International journal of radiation oncology, biology, physics* 34.2, pp. 497–505.

Vuong, T., S. Devic, and E. Podgorsak (2007). "High Dose Rate Endorectal Brachytherapy as a Neoadjuvant Treatment for Patients with Resectable Rectal Cancer". In: *Clinical Oncology* 19.9, pp. 701–705. DOI: 10.1016/j.clon.2007.07.006.

Vuong, Té et al. (2010). "High dose rate endorectal brachytherapy for patients with curable rectal cancer". In: *Seminars in Colon and Rectal Surgery*. Vol. 21. 2. Elsevier, pp. 115–119.

Webster, Matthew J et al. (2013a). "Dynamic modulated brachytherapy (DMBT) for rectal cancer". In: *Medical physics* 40.1, p. 011718.

Webster, Matthew J et al. (2013b). "HDR brachytherapy of rectal cancer using a novel grooved-shielding applicator design". In: *Medical physics* 40.9, p. 091704.

Williamson, Jeffrey F (1987). "Monte Carlo evaluation of kerma at a point for photon transport problems". In: *Medical physics* 14.4, pp. 567–576.

World Cancer Research Fund (2020). *Colorectal cancer statistics*. https://www.wcrf.org/dietandcancer/cancer-trends/colorectal-cancer-statistics. Accessed: 2020-06-26.

Yang, Y and MJ Rivard (2011). "WE-A-BRB-08: Comparison of Brachytherapy Dose Distribution Using the Gamma-Index Method". In: *Medical Physics* 38.6Part31, pp. 3793–3793.